

The OLYMPUS Experiment

R. Alarcon, L.D. Ice

Arizona State University, Tempe, AZ, USA

F. Brinker, N. D'Ascenzo, N. Goerrissen, J. Hauschildt, Y. Holler, D. Lenz,
U. Schneekloth

Deutsches Elektronen-Synchrotron, Hamburg, Germany

D. Bayadilov, R. Beck, D. Eversheim, Ch. Funke, Ph. Hoffmeister,
P. Klassen, A. Thiel

Rheinische Friedrich Wilhelms Universität Bonn, Bonn, Germany

O. Ates, J. Diefenbach, M. Kohl

Hampton University, Hampton, VA, USA

R. De Leo, R. Perrino

Istituto Nazionale di Fisica Nucleare, Bari, Italy

V. Carassiti, G. Ciullo, M. Contalbrigo, P. Lenisa, M. Statera
Universita' di Ferrara and Istituto Nazionale di Fisica Nucleare, Ferrara, Italy

E. Cisbani, S. Frullani

Istituto Nazionale di Fisica Nucleare, Rome, Italy

B. Glaeser, D. Khanefit, Y. Ma, F. Maas, R. Pérez Benito,
D. Rodríguez Piñeiro

Johannes Gutenberg Universität, Mainz, Germany

J.C. Bernauer, J. Bessuille, B. Buck, T.W. Donnelly, K. Dow, D.K. Hasell*,
B. Henderson, J. Kelsey, R. Milner, C. O'Connor, R.P. Redwine,
R. Russell, A. Schmidt, C. Vidal, A. Winnebeck

*Corresponding Author

Email address: hasell@mit.edu (D.K. Hasell)

¹Also with Universita' di Ferrara and Istituto Nazionale di Fisica Nucleare, Ferrara, Italy

Massachusetts Institute of Technology, Cambridge, MA, USA

V.A. Andreev, S. Belostoski, G. Gavrilov, A. Izotov, A. Kiselev,
A. Krivshich, O. Miklukho, Y. Naryshkin, D. Veretennikov

Petersburg Nuclear Physics Institute, Gatchina, Russia

R. Kaiser, I. Lehmann, S. Lumsden, M. Murray, G. Rosner, B. Seitz

University of Glasgow, Glasgow, United Kingdom

J.R. Calarco

University of New Hampshire, Durham, NH, USA

N. Akopov, A. Avetisyan, G. Elbakian, G. Karyan, H. Marukyan,
A. Movsisyan¹, H. Vardanyan, V. Yeganov

Yerevan Physics Institute, Yerevan, Armenia

Abstract

OLYMPUS was designed to measure the cross section ratio of positron-proton to electron-proton elastic scattering, with the goal of determining the contribution of two-photon exchange to elastic scattering. Two-photon exchange might resolve the discrepancy between measurements of the proton's form factor ratio $\mu_p G_E^p / G_M^p$ made using polarization techniques and those made in unpolarized experiments. To make this determination, OLYMPUS operated on the DORIS storage ring at DESY, alternating between electron and positron beams at 2.01 GeV incident on an internal hydrogen gas target. The experiment used a toroidal magnetic spectrometer instrumented with drift chambers and time of flight detectors to measure rates for elastic scattering over the polar angular range of approximately 25° – 75° . A symmetric Møller / Bhabha calorimeter at 1.29° and telescopes of GEM and MWPC detectors at 12° served as luminosity monitors. A total luminosity of approximately 4.4 fb^{-1} was collected over two running periods in 2012. This paper provides details on the accelerator, target, detectors, and operation of the experiment.

Keywords: elastic electron scattering, elastic positron scattering, two-photon exchange, form-factor ratio

2010 MSC: 25.30.Bf, 25.30.Hm, 13.60.Fz, 13.40.Gp, 29.30.-h

1. Introduction

Electron scattering has long been an important tool for studying the structure of nucleons. The strength of the technique lies in the predominantly electromagnetic nature of the interaction. The electron is simply a point-particle, and its vertex is well described by quantum electrodynamics. The interaction is mediated by a photon, whose momentum transfer sets a size scale for the structures that are probed in the scattering reaction. A low-momentum photon can only “see” the size of the nucleon, but by increasing the momentum, the photon is sensitive to the nucleon’s internal distribution of charge and magnetism, parameterized by form factors G_E and G_M . At even higher momentum transfers, deep inelastic scattering reveals the distributions of the quarks and gluons, which are ultimately responsible for the observed form factors. The synthesis of data at all different momentum scales can verify and guide our theoretical understanding of the nucleon.

Polarized beams and targets offer another window into the structure of nucleons. Recently, measurements of the electric to magnetic form factor ratio of the proton, $\mu_p G_E^p / G_M^p$, using polarization techniques (1–8) have shown a dramatic discrepancy in comparison with the ratio obtained using the traditional Rosenbluth technique in unpolarized cross section measurements (9–12) as shown in Fig. 1. This discrepancy might arise from a significant contribution to the elastic electron-proton cross section from hard two-photon exchange (13–18), a process which is neglected in the standard radiative corrections procedures. Since there is not a theoretical consensus on the size of this contribution (13–24), definitive measurements are needed to determine if two-photon exchange resolves the form factor discrepancy.

To address this question, the OLYMPUS Experiment was proposed to measure the ratio between the positron-proton and electron-proton elastic scattering cross sections. In the single-photon exchange approximation, this ratio is unity, while the next-to-leading interference of one-photon and two-photon exchange diagrams changes sign between electron and positron scattering. Measurements from the 1960s indicated some deviation in the ratio from unity, but the uncertainties were large, as can be seen in in Fig. 2.

The OLYMPUS experiment was approved for three months of dedicated operation at the DORIS electron/positron storage ring at DESY, in Hamburg, Germany. Alternating electron and positron beams were directed on a fixed proton target, with the scattered leptons and recoiling protons detected in coincidence over a wide range of scattering angles. An unpolarized hydro-

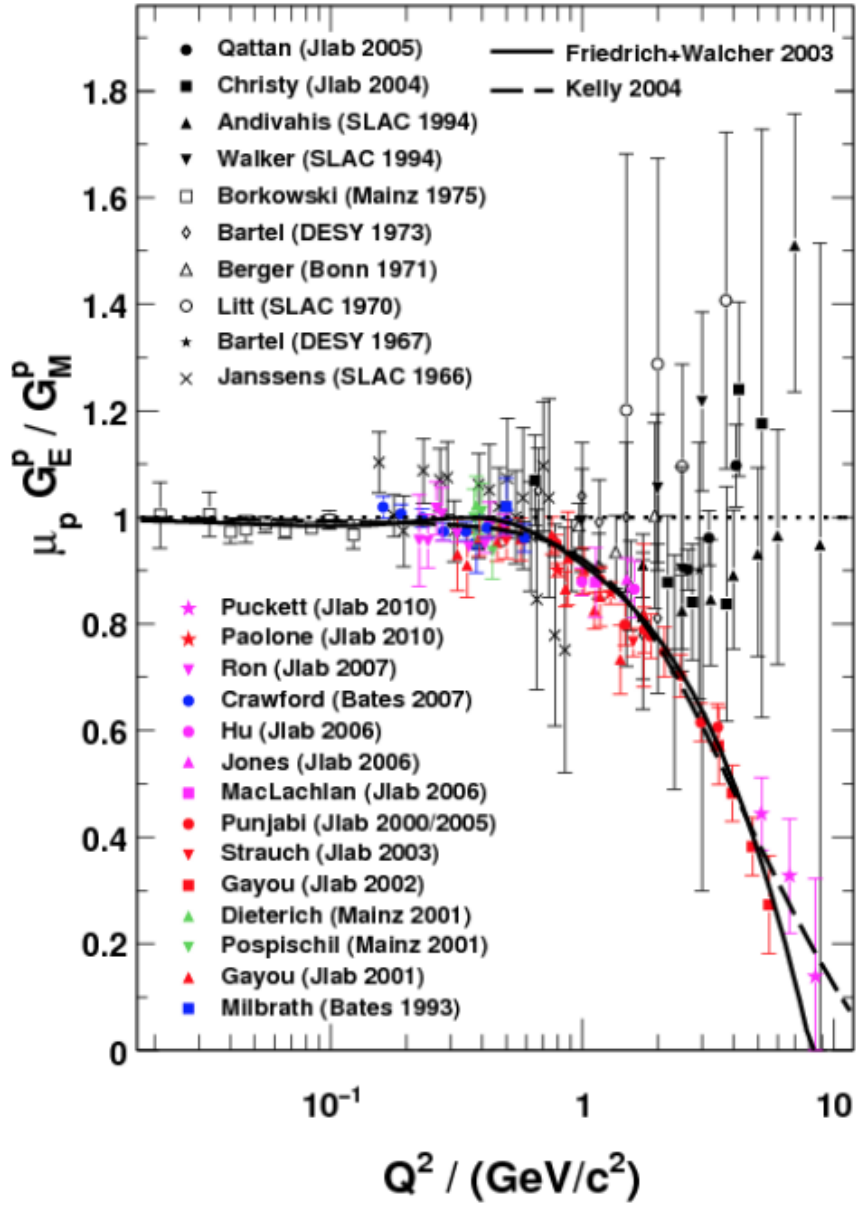


Fig. 1: Ratio of proton form factors $\mu_p G_E^p / G_M^p$ as a function of Q^2 showing results from unpolarized measurements in black and recent data measured using polarized techniques.

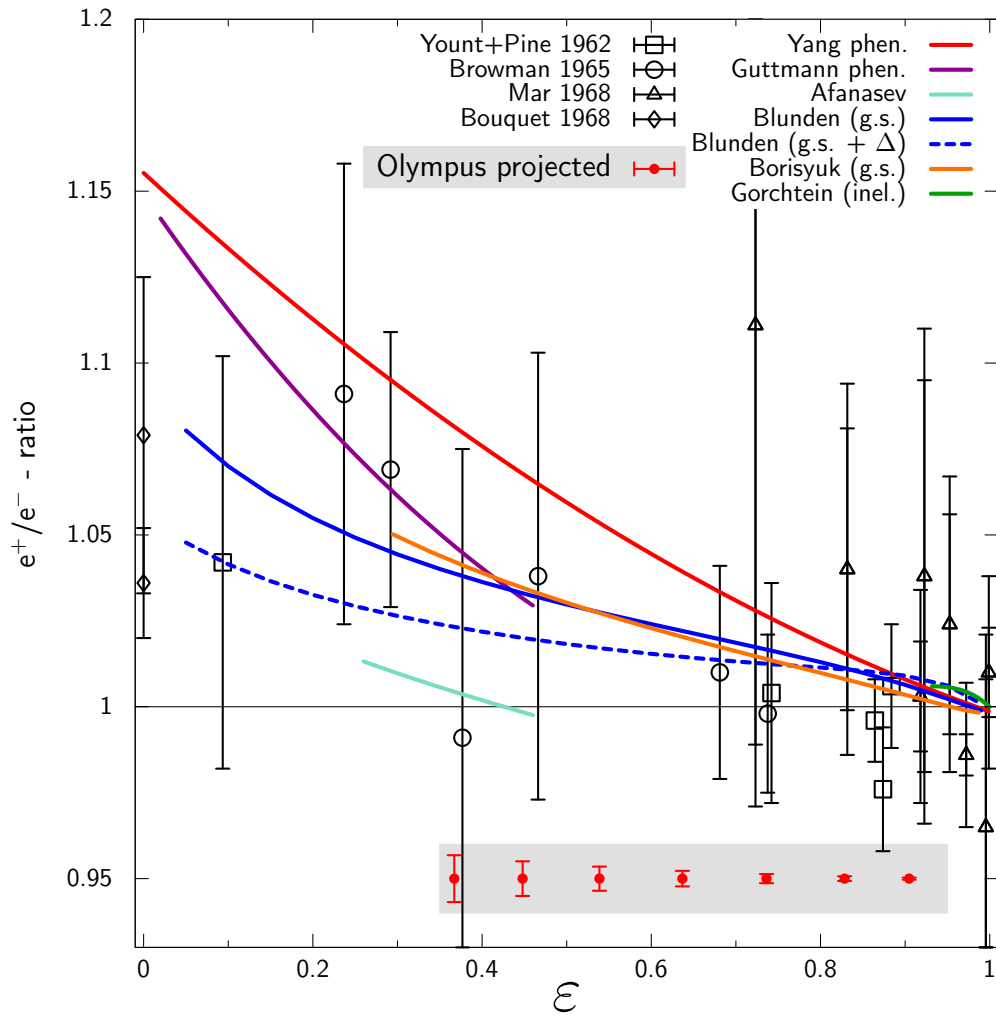


Fig. 2: Ratio of positron to electron elastic scattering cross section as a function of ϵ showing existing data, some theoretical predictions, and projected OLYMPUS data range and uncertainties. Theory calculations are from (16–18, 21–24).

38 gen gas target was designed and built at MIT and installed internally to the
39 DORIS ring. The former BLAST detector was shipped from MIT-Bates to
40 DESY and placed around the target. The detector used a toroidal magnetic
41 field with a left/right symmetric arrangement of tracking detectors and time
42 of flight scintillators. In addition, three new detector systems were designed
43 and built to monitor the luminosity during the experiment; triple GEM de-
44 tectors from Hampton and MWPC detectors from PNPI were mounted in
45 telescopes at 12° , while symmetric Møller/Bhabha calorimeters from Mainz
46 were positioned at 1.29° . The Bonn group provided the software and hard-
47 ware for the data acquisition system. The trigger and slow control systems
48 were developed by MIT.

49 The OLYMPUS Experiment collected data in two periods: the February
50 period (January 20 - February 27, 2012) and the Fall period (October 24,
51 2012 - January 2, 2013). During the February period, the beam species was
52 typically changed daily, and the magnet polarity was changed randomly, but
53 equally, every 6 hours. For the February data run, there was a leak in the
54 target gas supply such that only a fraction of the measured flow reached
55 the target cell. Because of this, a lower than expected luminosity was ob-
56 tained. The gas leak was repaired in the summer so that it was possible to
57 achieve high luminosity in the Fall period. However, it was discovered that
58 at high luminosity and negative magnet polarity too many electrons were
59 bent into the wire chambers, preventing their operation. After several tests
60 and attempts to remedy this, it was decided to operate at high luminosity
61 but primarily with positive magnet polarity for most of the Fall period.

62 The following sections describe the accelerator, target, detectors, data
63 acquisition, and operation in more detail.

64 2. DORIS Storage Ring at DESY

65 The DORIS storage ring at DESY originally began operation in 1974 as an
66 electron-electron and electron-positron collider. After its long and successful
67 operation for particle physics research, DORIS was dedicated to synchrotron
68 radiation studies in 1993. Since DORIS had access to both a positron and
69 electron source and could circulate both species at several GeV energies, it
70 was a natural candidate for the OLYMPUS experiment. Additionally, the
71 infrastructure at the location in the beamline of the former Argus Experiment
72 (25) provided an excellent match to the size and needs of OLYMPUS. In 2009,
73 the shutdown of DORIS was scheduled for the end of 2012, placing a tight
74 time constraint on OLYMPUS.

75 Although the DORIS accelerator and the ARGUS detector site were well
76 suited to the OLYMPUS Experiment, several modifications were required.
77 In particular, a number of considerations were necessary to allow DORIS
78 to continue to operate as a synchrotron light source after OLYMPUS was
79 installed (although not during OLYMPUS data taking). These included:

- 80 - RF cavities that had been installed at the detector site had to be re-
81 located 26 m upstream.
- 82 - An additional quadrupole was installed on each side (± 7 m) of the
83 OLYMPUS interaction region to reduce the beam size for the OLYM-
84 PUS target while not significantly affecting the beam profile in syn-
85 chrotron radiation source elements. This was necessary due to the
86 impracticality of removing the OLYMPUS target for synchrotron runs.
- 87 - The OLYMPUS target required cooling during synchrotron radiation
88 runs due to the wakefield heating caused by the 150 mA, 4.5 GeV,
89 5-bunch beam.
- 90 - A number of tests and improvements were required to achieve the 10-
91 bunch, 2.01 GeV beam conditions for OLYMPUS operation with ade-
92 quate currents and lifetimes, including the implementation of a multi-
93 bunch feedback system.

94 A key feature of the OLYMPUS experiment was the frequent switching
95 between e^- and e^+ beams. The DORIS pre-accelerators were already able
96 to switch between electrons and positrons within approximately 10 minutes,
97 but the extraction from the pre-accelerators to DORIS, the transport line,
98 and the DORIS ring needed several modifications:

- 99 - The high voltage pulse power supplies for the pre-accelerator extraction
100 and the DORIS injection kickers had to be rebuilt.
- 101 • The septa magnets for pre-accelerator extraction and DORIS injection
102 were modified to serve as bipolar devices.
 - 103 • Remotely-controlled polarity switchers for a number of 800 A magnet
104 power supplies had to be constructed and installed

105 The daily switching of the beam species for OLYMPUS posed a challenge
106 for the parallel operation of DORIS and the PETRA storage ring, which
107 shared the same pre-accelerators. While PETRA did not operate during the
108 February run, the procedure for switching the polarity of the pre-accelerators
109 was optimized to accommodate parallel operation during the Fall run. With
110 these improvements, PETRA could be refilled in approximately five minutes,
111 causing only a small delay for DORIS refills.

112 Since the injection into DORIS occurred at full energy, it was possible
113 to run in top-up mode to achieve higher average current, and hence more
114 luminosity. The injection process was optimized to minimize beam losses,
115 which prevented excessive rates in the OLYMPUS detector (which would
116 cause high voltage trips).

117 The radiation levels in the region downstream of the experiment increased
118 when gas was added to the target, and additional shielding was installed to
119 account for this. Also, the beam scrapers upstream of the experiment were
120 optimized to minimize the noise rates in the experiment.

121 To monitor the beam energy, a dipole reference magnet was installed in
122 series with the DORIS dipole magnets. This magnet included a rotating
123 coil to measure the integrated field strength. The accelerator archive system
124 monitored all relevant data, power supply currents for all magnets, beam
125 position data, scraper positions, etc. and provided much of this information
126 to the OLYMPUS slow control system.

127 **3. Target and Vacuum Systems**

128 The OLYMPUS experiment used an unpolarized, internal hydrogen gas
129 target cooled to below 70 K. The hydrogen gas flowed into an open-ended,
130 600 mm long, elliptical target cell (Sec. 3.1). The target cell was housed in
131 a scattering chamber (Sec. 3.2) that had thin windows to match the angular
132 acceptance of the detectors. A tungsten collimator (Sec. 3.4) was also housed
133 in the scattering chamber to prevent synchrotron radiation, beam halo, and
134 off-momentum particles from striking the target cell. Additionally, a series of
135 wakefield suppressors (Sec. 3.3) were necessary to reduce the heat load on the
136 target cell. Finally, an extensive vacuum system (Sec. 3.5) of turbomolecular
137 and Non-Evaporable Getter (NEG) pumps was employed to preserve the
138 vacuum in the DORIS storage ring.

139 *3.1. Target Cell*



Fig. 3: Photograph of one of the OLYMPUS target cells mounted inside the scattering chamber.

140 The target cell consisted of an open-ended, elliptical cylinder (27 mm
141 horizontal \times 9 mm vertical \times 600 mm long) made from 0.075 mm thick alu-
142 minium. The elliptical shape was chosen to match the DORIS beam envelope
143 and was set to approximately the 10σ nominal horizontal and vertical beam

144 width at the OLYMPUS interaction point to minimize the amount of beam
145 halo striking the cell walls.

146 Several cells were fabricated over the course of the experiment at INFN,
147 Ferrara. Cells were formed from two identical stamped sheets of aluminum
148 that were spot welded together along the top and bottom seams. Each cell
149 was mounted in a frame by a clamp that ran the entire length of the top seam.
150 The frame was made of 6063 aluminum to provide high thermal conductivity
151 at cryogenic temperatures. When installed in the scattering chamber, the cell
152 and frame assembly was suspended from a flange in the top of the scattering
153 chamber (shown in Fig. 3) and its position and orientation could be adjusted.
154 The entire cell and frame assembly were cooled by a cryogenic coldhead. The
155 assembly was wrapped in several layers of aluminized mylar to insulate it
156 from thermal radiation. Without beam or gas flow, the target could reach
157 temperatures below 40 K. During high luminosity running, a temperature of
158 about 70 K was sustained.

159 During operation, hydrogen gas was flowed through the target cell. The
160 hydrogen gas was produced by a commercial hydrogen generator and was
161 controlled by a series of valves, buffer volumes, and mass flow controllers.
162 The gas entered the cell at the center, from a tube that fit snugly into
163 an opening of the cell's top seam. The gas diffused outwards to the open
164 ends of the cell, where it was removed by the vacuum system. This diffusion
165 was slowed because the hydrogen quickly cooled to the temperature of the
166 cell. The density distribution in the cell was triangular, with peak density
167 at the center of the cell falling to zero density at either end. A flow rate of
168 1.5×10^{17} H₂ atoms per second was required to produce a target thickness
169 of 3×10^{15} atoms cm⁻².

170 *3.2. Scattering Chamber*

171 The OLYMPUS scattering chamber (shown in Fig. 4) was 1.2 m long
172 and was machined from a solid block of aluminum, with large area windows
173 on the left and right faces. The windows were made of 0.25 mm thick 1100
174 aluminum, and nominally subtended a polar angular range of 8° to 100° from
175 the center of the target, 6° to 90° from 200 mm upstream, and 10° to 120°
176 from 200 mm downstream. The chamber was trapezoidal in shape to angle
177 the windows forward to make more of the target cell “visible” to the 12°
178 detectors.

179 In addition to windows, the chamber had ports for the beamline (up-
180 and downstream), for pumping (on the bottom surface), and for access to

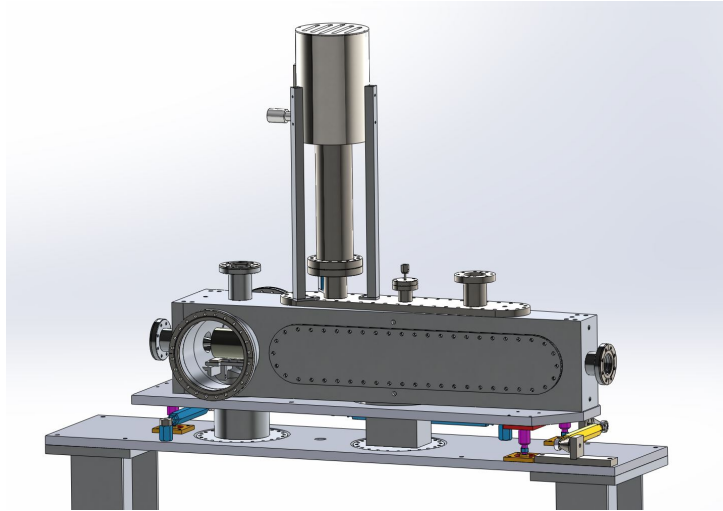


Fig. 4: CAD model of the OLYMPUS scattering chamber.

181 the collimator (on the left and right), as well as the target cell flange on the
 182 top, which had feedthroughs for the hydrogen gas, the coldhead, and various
 183 sensors. The main components inside the scattering chamber are shown in
 184 Fig. 5.

185 *3.3. Wakefield Suppressors*

186 Wakefield suppressors were necessary to maintain the target cell at cryo-
 187 genic temperatures by preventing heating caused by wakefields. The wake-
 188 field suppressors consisted of conducting transitions that were added to fill
 189 gaps between conducting structures surrounding the beam. Any sharp tran-
 190 sitions or gaps in conductivity would serve as electrical cavities that would
 191 be excited by the passing beam, creating wakefields and producing heat. To
 192 prevent this, three wakefield suppressors were produced to cover the following
 193 transitions:

- 194 1. from the circular upstream scattering chamber port (60 mm in diame-
 195 ter) to the 25 mm by 7 mm elliptical opening of the collimator,
- 196 2. from the exit of the collimator to the entrance of the target cell (both
 197 27 mm by 9 mm ellipses), and
- 198 3. from the 27 mm by 9 mm elliptical exit of the target cell to the circular
 199 downstream scattering chamber port (60 mm in diameter).

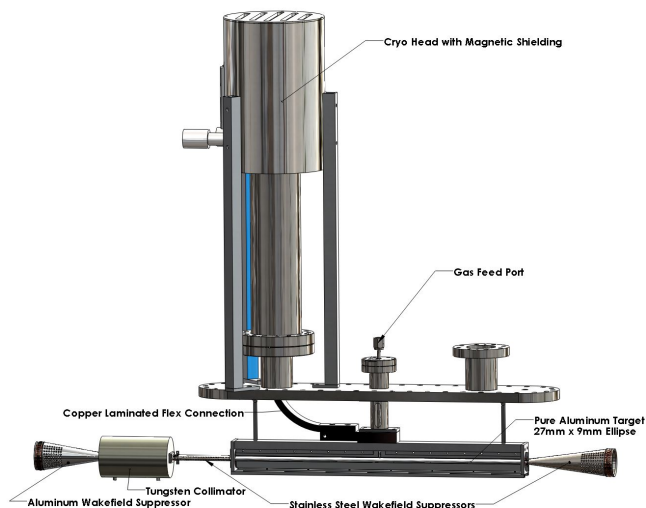


Fig. 5: CAD model of the target cell, wakefield suppressors, and collimator inside the OLYMPUS scattering chamber.

200 With these wakefield suppressors, a target temperature of around 50 K could
 201 be maintained during synchrotron operation, and a temperature less than
 202 70 K could be maintained during high-luminosity OLYMPUS running.

203 The wakefield suppressors were made of stainless steel (except the up-
 204 stream wakefield suppressor, which was made of aluminum), and plated with
 205 silver for improved electrical conductivity. The surfaces were smooth except
 206 for many small holes, which were drilled to allow the vacuum system to pump
 207 gas through them. The ends of the wakefield suppressors had beryllium-
 208 copper spring fingers around their circumference. These spring fingers made
 209 sliding connections at an interface that allowed for thermal expansion while
 210 maintaining good electrical contact. The upstream wakefield suppressor was
 211 screwed directly to the collimator, while making a sliding connection with
 212 the upstream scattering chamber port. The other two wakefield suppressors
 213 were fixed to rings clamped to the ends of the target, and made sliding con-
 214 nections to either the downstream scattering chamber port or the collimator.
 215 A close up view of the middle wakefield suppressor is shown in Fig. 6).

216 3.4. Collimator

217 Fig. 6 also shows the fixed collimator in front of the target cell. The
 218 collimator consisted of a 139.7 mm long cylinder of tungsten 82.55 mm in

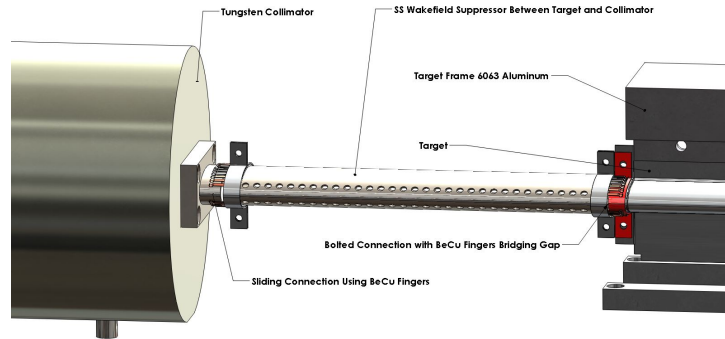


Fig. 6: CAD model of the wakefield suppressor between the collimator and the target cell.

219 diameter. The outer dimensions were chosen after performing a study on sim-
 220 ulated showers of beam-halo particles. It had a tapered elliptical aperture
 221 with entrance 25 mm by 7 mm and exit 27 mm by 9 mm. The collimator was
 222 machined from a solid block of tungsten using wire electrical discharge ma-
 223 chining, EDM². The entrance dimensions were chosen to be slightly smaller
 224 than those of the storage cell to shield the target cell walls.

225 3.5. Vacuum System

226 A system of magnetic levitation turbomolecular pumps³ (800 l/s capac-
 227 ity) and NEG pumps⁴ (400 l/s capacity) were used to pump the section
 228 of beamline inside the OLYMPUS experiment. This system utilized three
 229 stages of pumping to reduce the pressure from the relatively high pressure
 230 ($\sim 10^{-6}$ Torr) at the scattering chamber (caused by hydrogen gas) to the low
 231 pressure ($\sim 10^{-9}$ Torr) of the DORIS storage ring.

232 The vacuum system is shown in Fig. 7. Six turbomolecular pumps (mod-
 233 els Osaka TG 1100M and Edwards STP 1003C) formed a differential pumping
 234 system to prevent hydrogen in the target from contaminating the vacuum of
 235 the storage ring. Two turbo pumps located in the pit directly beneath the ex-
 236 periment were directly connected to the scattering chamber through 200 mm

²Jack's Machine Co. Hanson, MA 02341

³Osaka and Edwards

⁴SAES Capacitor CFF 4H0402

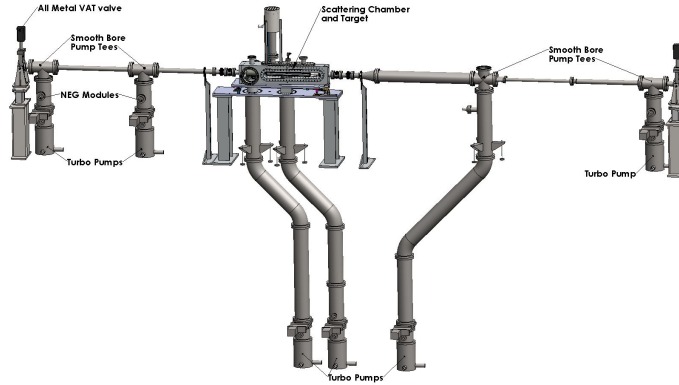


Fig. 7: CAD model of the vacuum system employed on the OLYMPUS experiment.

237 diameter pipes. Two more turbo pumps were connected to the up- and down-
238 stream beamlines approximately 2 m from the target. At approximately 3 m
239 from the target another two turbo pumps were used to reduce the pressure
240 in the beamline to the level acceptable for the DORIS storage ring. The four
241 pumping stations furthest from the target also had NEG pumps to improve
242 the pumping of hydrogen.

243 4. The OLYMPUS Detector

244 The core of the OLYMPUS detector consisted of components from the
245 BLAST spectrometer from MIT-Bates (26). The toroidal magnet, time-of-
246 flight detectors, and many of the readout and control electronics were shipped
247 to DESY in Spring 2010. The components were reassembled, reconditioned,
248 and modified as necessary for installation in OLYMPUS detector.

249 The OLYMPUS Experiment was installed in the straight section of the
250 DORIS storage ring, in the location of the former ARGUS Experiment (25).
251 The initial assembly took place from June, 2010 to July, 2011 outside of the
252 DORIS tunnel, to avoid interfering with DORIS operation. The detector
253 was assembled on a set of rails that led (through a removable shielding wall)
254 to the ARGUS site. When the assembly was complete, the shielding wall
255 was removed, the spectrometer was rolled into place in the tunnel, and the
256 wall was rebuilt. The experimental site was 7 m wide, with a 5 m deep
257 pit below the beam height. The pit was a convenient location for vacuum
258 pumps, power supplies, and the target gas low system because it was deep
259 enough to be outside of the fringes of the magnet field.

260 In the area outside the shielding wall was an electronics “hut,” which was
261 supported on the same set of rails. The hut housed the detectors’ readout
262 and control electronics, the high voltage supplies, and the computer systems,
263 and could be accessed even when the DORIS beam was circulating.

264 The OLYMPUS spectrometer consisted of an eight-coil toroidal magnet
265 with detector instrumentation in the two sectors of the horizontal plane of
266 the beamline (see Fig. 8). Each of these sectors contained a large drift cham-
267 ber for particle tracking and an array of time-of-flight scintillator bars for
268 trigger timing and rough energy and particle position measurements. To
269 monitor the luminosity, OLYMPUS had a redundant system of a Symmetric
270 Møller/Bhabha (SYMB) calorimeter at $\theta = 1.29^\circ$ and detector telescopes
271 consisting of three triple gas electron multiplier (GEM) detectors interleaved
272 with three multi-wire proportional chambers (MWPCs) at 12° in both sec-
273 tors.

274 The following sections describe the detector components in greater detail.

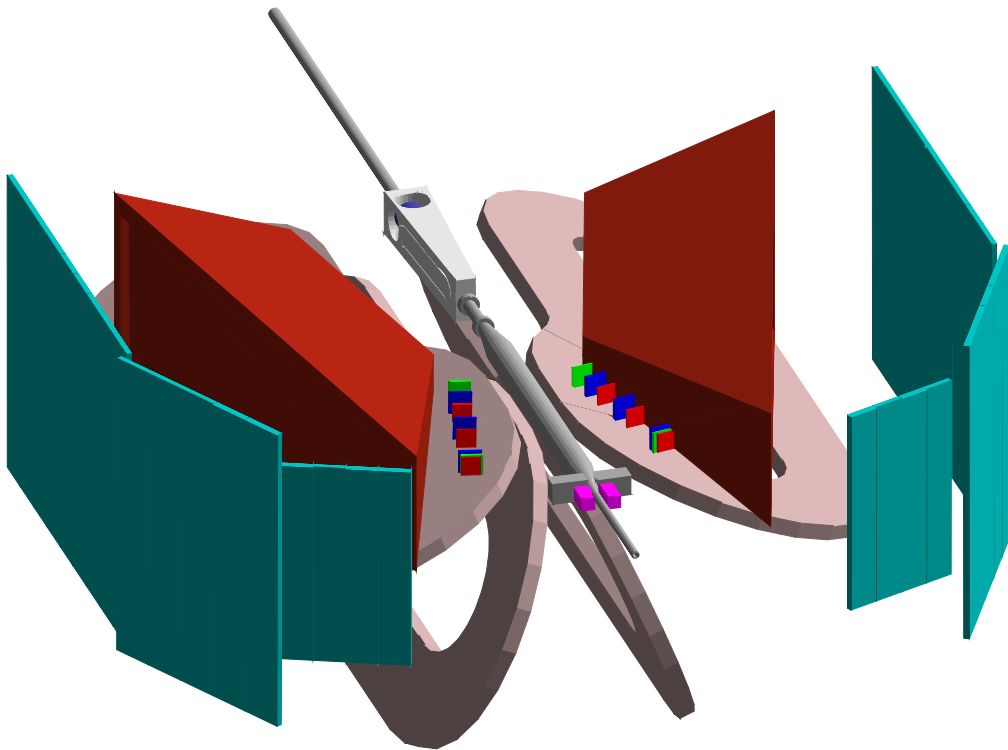


Fig. 8: A solid-model representation of the OLYMPUS detector with the top four magnet coils removed to show the instrumented horizontal sectors.

275 *4.1. Toroidal Magnet*

276 The toroidal magnet consisted of eight copper coils placed around the
277 beam line and scattering chamber so that the beam traveled down the toroid's
symmetry axis (see Fig. 9). The coils divided the space around the beamline

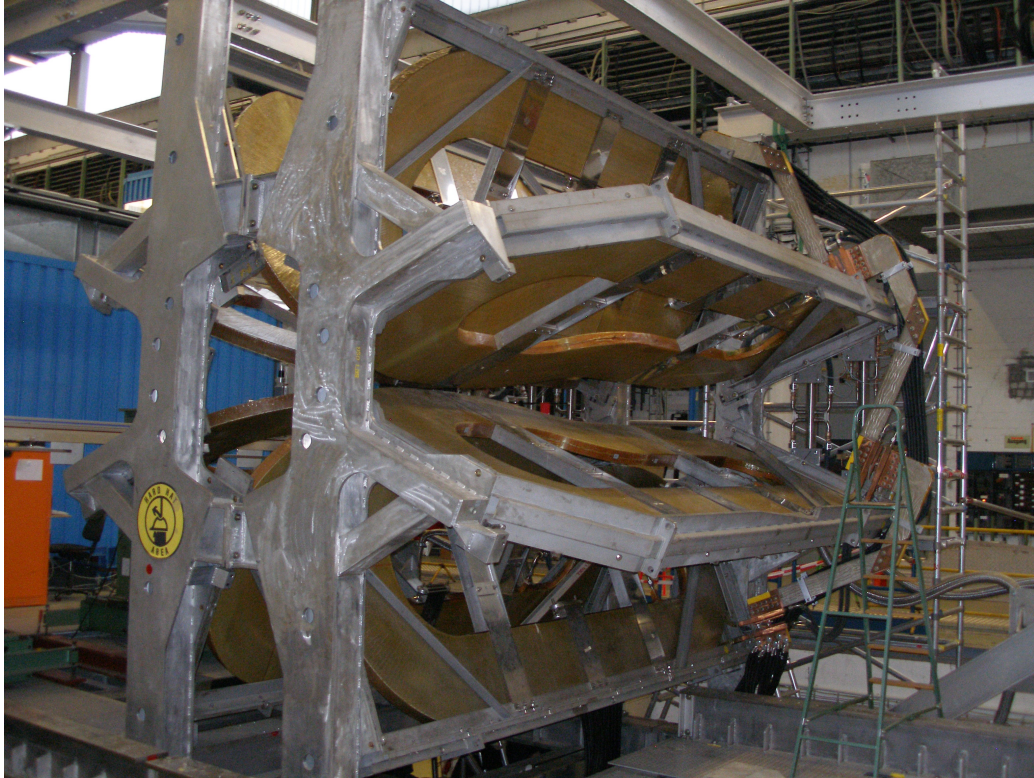


Fig. 9: The toroid magnet assembled at DESY before the subdetectors were installed

278
279 into eight sectors. The two sectors in the horizontal plane were instrumented
280 with detectors. During normal operation, the magnet produced a field of
281 about 0.28 T in the region of the tracking detectors.

282 The magnet was originally designed and used for the BLAST experiment,
283 and has been described in a previous article (27). The choice of a toroidal
284 configuration was made to ensure a small field along the beamline in order to
285 minimize any effects on a spin-polarized beam and to limit field gradients in
286 the region of the polarized target. Since OLYMPUS used neither a polarized
287 beam nor a polarized target, these concerns were not as important. However,
288 during the initial set-up, the magnetic field along the beamline was measured

289 and the coil positions adjusted to achieve an integrated field $< 0.005 \text{ T}\cdot\text{m}$ to
 290 avoid perturbing the beam's position or direction.

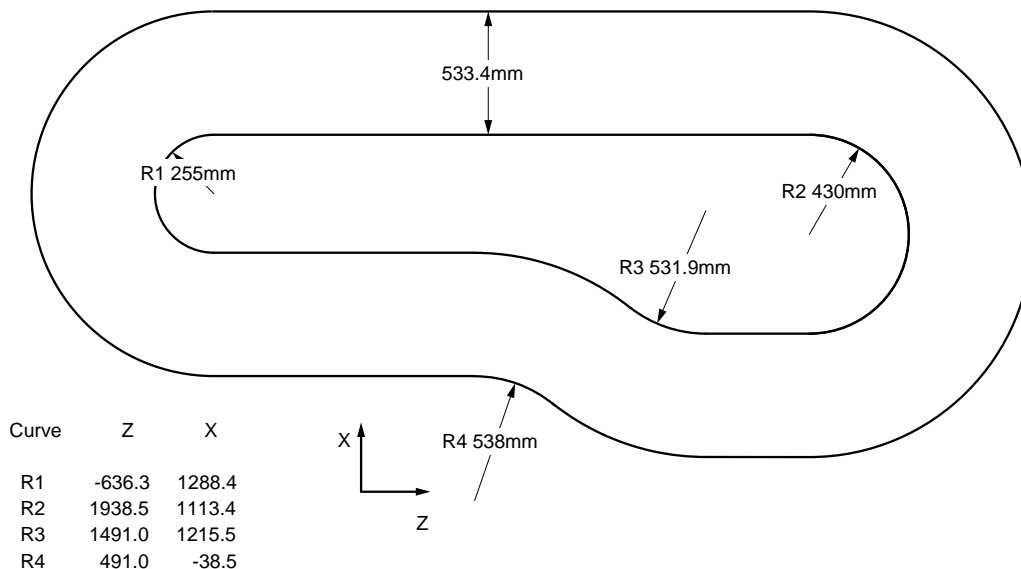


Fig. 10: Plan view of BLAST coil outline showing dimensions and position relative to the center of the target cell.

291 Each of the toroid's eight coils consisted of 26 turns of 1.5 inch square
 292 copper tubes, organized into two layers of 13 turns. A circular hole, 0.8 inches
 293 in diameter, ran down the length of each tube and served as a conduit for
 294 cooling water. During assembly, the tubes were individually wrapped with
 295 fiberglass tape and then collectively potted in an epoxy resin matrix. The
 296 final outline and nominal position relative to the beam line and target center
 297 at the coordinate origin are shown in Fig. 10. The coils are narrower at one
 298 end to accommodate the scattering chamber and wider at the other to extend
 299 the high-field region to more forward angles, where scattered particles have
 300 higher momenta.

301 The magnetic field served two purposes. The first was to bend the tracks
 302 of charged particles, allowing their momentum and charge sign to be deter-
 303 mined from the curvature of their tracks. The second was to sweep away low-
 304 energy, charged background particles from the tracking detectors. Though
 305 a stronger magnetic field would have improved momentum resolution and
 306 reduced the background, it would also have increased the Lorentz angle of
 307 drift electrons in the tracking detectors, making track reconstruction more

308 difficult. A balance was struck by choosing a current of 5000 A for normal
309 operation, which produced a field of about 0.28 T in the high-field regions.

310 Originally, it was planned to alternate the polarity of the magnet every
311 few hours to reduce systematic uncertainties. However, this proved imprac-
312 tical at high-luminosity. In the negative polarity setting, the magnet bent
313 negatively charged particles outward from the beamline. The drift chambers
314 were hit with large background of low-energy electrons, which frequently
315 caused the high-voltage supply to exceed its current threshold and deacti-
316 vate. Attempts to adequately shield the drift chambers, both by adding
317 material and by increasing the magnetic field strength, were unsuccessful.
318 Consequently, the negative polarity setting was limited to low-luminosity
319 running, and only about 13 % of the total luminosity was collected in this
320 mode. The limited negative polarity data will provide a check on systematic
321 uncertainties.

322 After the experimental running period was completed, the drift cham-
323 bers, the 12° luminosity monitors, the Møller detector, and the beamline
324 downstream of the scattering chamber were removed in order to conduct a
325 measurement of the magnetic field. The field region was scanned using a
326 3D Hall probe mounted to a rod, driven by several translation tables. The
327 rod was mounted to a long XYZ table with a range of motion of 0.2 m by
328 0.2 m by 6 m. (By convention, the direction of the beam was labeled as
329 the OLYMPUS Z -axis, the Y -axis pointed up, and the X -axis pointed to-
330 ward the left sector, forming a right-handed coordinate system.) This long
331 table was supported by two large XY tables that augmented the X and Y
332 ranges each by 1 m. The range of motion was further extended in X by
333 substituting rods of different lengths and in Y by adding a vertical extension
334 piece. The apparatus was used to measure the field over a grid of points
335 on the left sector, before being transported and reassembled for a similar
336 measurement of points on the right sector. The grid extended from -0.5 m
337 to 3.5 m in Z . In X and Y , the grid was limited to the triangular space
338 between the coils, but extended to ± 2.7 m on either side of the beamline.
339 The grid points were spaced 0.05 m apart in the region within 1 m of the
340 beamline, and 0.10 m apart in the outer region, where the field changed less
341 rapidly. In total, approximately 35,000 positions were measured, including
342 the downstream beamline region, which was measured redundantly from the
343 left and the right.

344 After the initial setup of the apparatus, the precise position of the XYZ
345 tables was measured with a laser tracking station over the course of a typical

346 scan in Z . This showed that the Hall probe position varied in X and Y as a
 347 function of Z during a scan, but that the shape was quite reproducible. To
 348 correct for this variation, the start and end points of each scan were measured
 349 using a theodolite and a total station. This data then allowed the position
 350 of the Hall probe to be determined for each measurement.

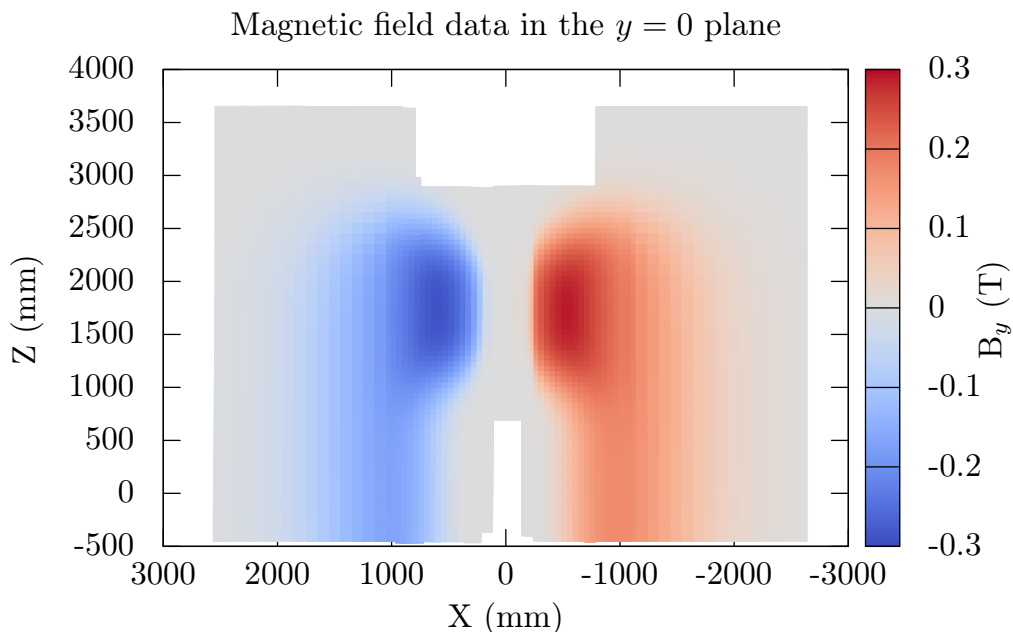


Fig. 11: The data from the magnetic field measurements in horizontal plane as viewed from above

351 After correcting the Hall probe positions, a fit was performed to the
 352 magnetic field data. The fit was based on a model of the coil geometry
 353 with a Biot-Savart calculation of the magnetic field. The fit allowed the
 354 coil positions to vary slightly to best match the measurements. This model
 355 was then used to extrapolate the field over the entire volume around the
 356 OLYMPUS detector for use in track reconstruction and in the OLYMPUS
 357 Monte Carlo simulation.

358 *4.2. Drift Chambers*

359 The drift chambers used for the OLYMPUS experiment came from the
360 BLAST experiment at MIT-Bates and have been described in great detail
361 elsewhere (26), so the following description will be brief while mentioning
362 new and updated features.

363 The drift chambers were used to measure the momenta, charges, scatter-
364 ing angles, and vertices of out-going charged particles. This was achieved
365 by tracking those particles in three dimensions through the drift chambers,
366 which were positioned within the toroidal magnetic field. Reconstructing a
367 particle's trajectory backwards to the scattering vertex allowed the scattering
368 angles and vertex position to be determined. Measuring the curvature of a
369 trajectory yielded the particle's momentum, while the direction of curvature
370 indicated the sign of particle's charge. The drift chambers had a large angular
371 acceptance and nominally subtended a range of 20° – 80° in polar angle and a
372 $\pm 15^\circ$ range in azimuth. The chambers were oriented to be normal to a polar
373 angle of 73.54° . Because of these choices, the chambers were trapezoidal in
374 shape (see Fig. 12).

375 The drift chambers were arranged in two sectors that were positioned
376 on either side of the target, in the horizontal plane. Each sector contained
377 three drift chambers (inner, middle, and outer) joined together by two in-
378 terconnecting sections to form a single gas volume. Thus, only one entrance
379 and one exit window were needed, reducing multiple scattering and energy
380 loss. A cross sectional view of the top plate of one of the assembled gas vol-
381 umes is shown in Fig. 13. The drift chambers combined had approximately
382 10,000 wires, which were used to create the drift field. Of these, 954 were
383 sense wires, which read out the signals from ionization caused by a charged
384 particle track.

385 Each chamber consisted of two super-layers (or rows) of drift cells, with
386 20 mm separation between the super-layers. The drift cells were formed by
387 wires in a “jet style” configuration. Fig. 14 shows a cross-sectional view of a
388 portion of one chamber with the two super-layers of drift cells. It also shows
389 characteristic “jet-style” lines of electron drift in a magnetic field. Each drift
390 cell was $78 \times 40 \text{ mm}^2$ and had 3 sense wires staggered $\pm 0.5 \text{ mm}$ from the
391 center line of each cell to help resolve the left/right ambiguity in determining
392 position from the drift time. The wires in one super-layer were strung with
393 a 10° stereo angle relative to wires of the other so that each chamber could
394 localize a trajectory in three dimensions.

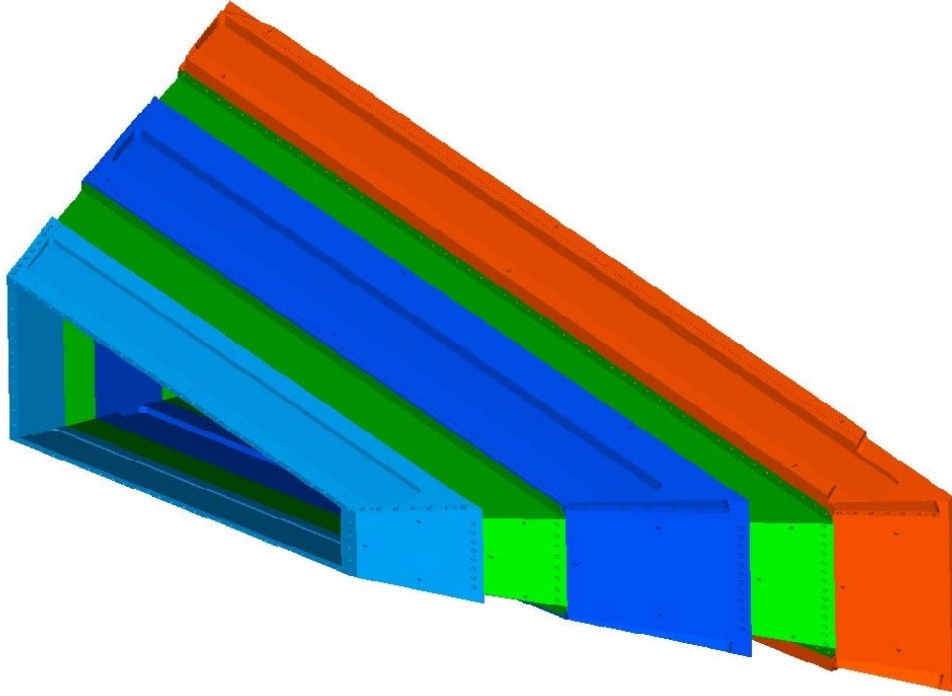


Fig. 12: Isometric view of all three drift chambers assembled into a single gas volume.

395 Because transporting the chambers in a way that would protect the
396 wires from breaking was infeasible, the chambers were unstrung before be-
397 ing shipped from MIT-Bates to DESY. The chambers were then completely
398 rewired in a clean room at DESY over a period of about three months during
399 the summer of 2010. In addition to new wires, improvements were made to
400 the front-end electronics, building on experience gained from BLAST.

401 For the experiment, an argon:carbon dioxide:ethanol gas mixture (87.4 :
402 9.7 : 2.9) was chosen for the drift chambers. The ethanol was added by
403 bubbling the argon:carbon dioxide gas mixture through a volume of liquid
404 ethanol kept at $\sim 5^\circ\text{C}$. The chambers were maintained at a pressure of ap-
405 proximately 1 inch of water above atmospheric pressure with a flow rate of
406 around 5 L/min.

407 Signals in the sense wires were processed with front-end electronics housed
408 in the recesses of the interconnecting sections before being sent to TDC mod-
409 ules in the electronics hut. The signals were first decoupled from the high-

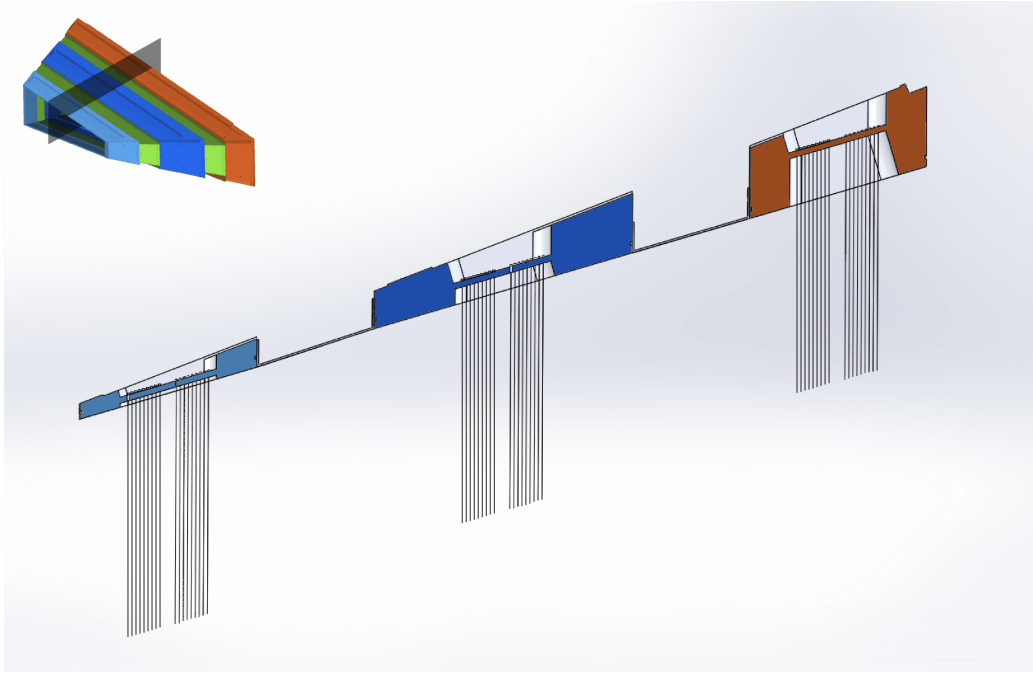


Fig. 13: Cross sectional view of the top plates of the three drift chambers and the two interconnecting sections when assembled into a single gas volume. The recesses between the top plates of the individual chambers housed front-end electronics and cables.

410 voltage on new, custom-designed, high-voltage distribution boards. The sig-
411 nals next passed to Nanometrics Systems⁵ N-277L amplifier/discriminators.
412 Then the signals were passed by Ethernet cable to the electronics hut, to
413 LeCroy⁶ 1877 Multihit TDC modules, operated in common-stop mode, with
414 the stop signal being provided by a delayed trigger signal. The digitized
415 signals were read out by the data acquisition system. An example TDC
416 spectrum for a single wire is shown in Fig. 15.

⁵Nanometric Systems, Berwyn, IL, USA

⁶Teledyne Lecroy, Chestnut Ridge, NY, USA

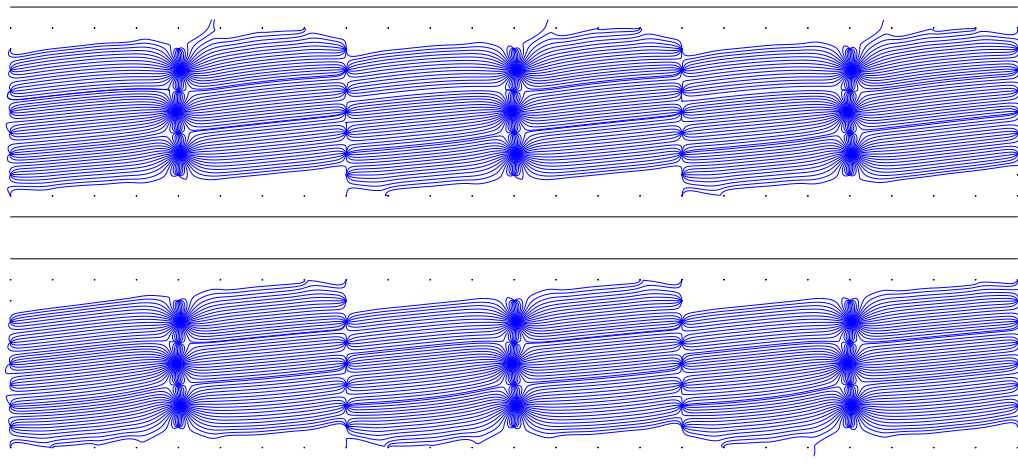


Fig. 14: Portion of a chamber showing the two super-layers of drift cells formed by wires. Lines of electron drift in the drift cells assuming a typical magnetic field around 3.0 kG are also shown.

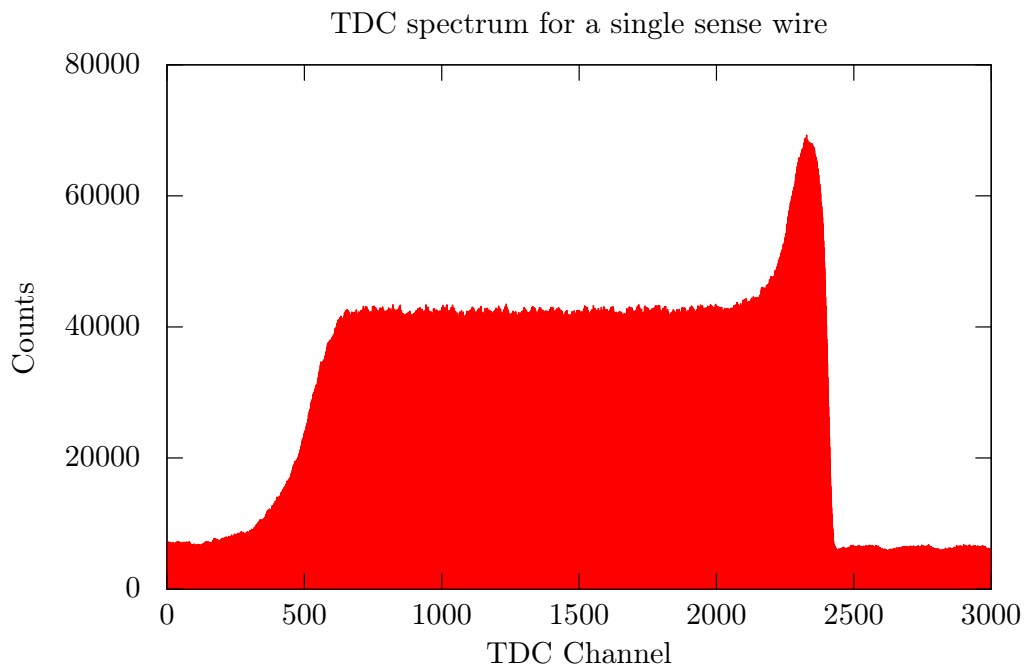


Fig. 15: A typical TDC spectrum for a single wire has a “church shape,” which is characteristic of jet-style drift chambers in common stop mode.

417 *4.3. Time of Flight Detectors*

418 The time-of-flight (ToF) detector was adapted from the system used for
419 the BLAST Experiment (26). Each sector consisted of 18 vertical scintillator
420 bars read out with photo-multiplier tubes (PMT) mounted at both ends, as
421 shown in Fig. 16. The four most-forward bars on each side were 119.4 cm
422 high, 15.2 cm wide, and 2.54 cm thick. The remaining 14 bars on each
423 side were 180.0 cm high, 26.2 cm wide, and 2.54 cm thick, so as to cover
424 the entire acceptance of the drift chambers. The Glasgow University group
425 designed and constructed a new support structure which allowed for the
426 tight arrangement and quick replacement of individual bars. allowing for a
427 tight arrangement and quick replacement of individual bars. The bars were
428 arranged in three planar sections oriented with their normal approximately
429 pointing toward the target area.

430 The ToF detector provided the timing signals used to trigger the readout
431 and data acquisition system for the majority of detector components. In
432 particular, it provided the common stop signal for the drift chamber TDCs.

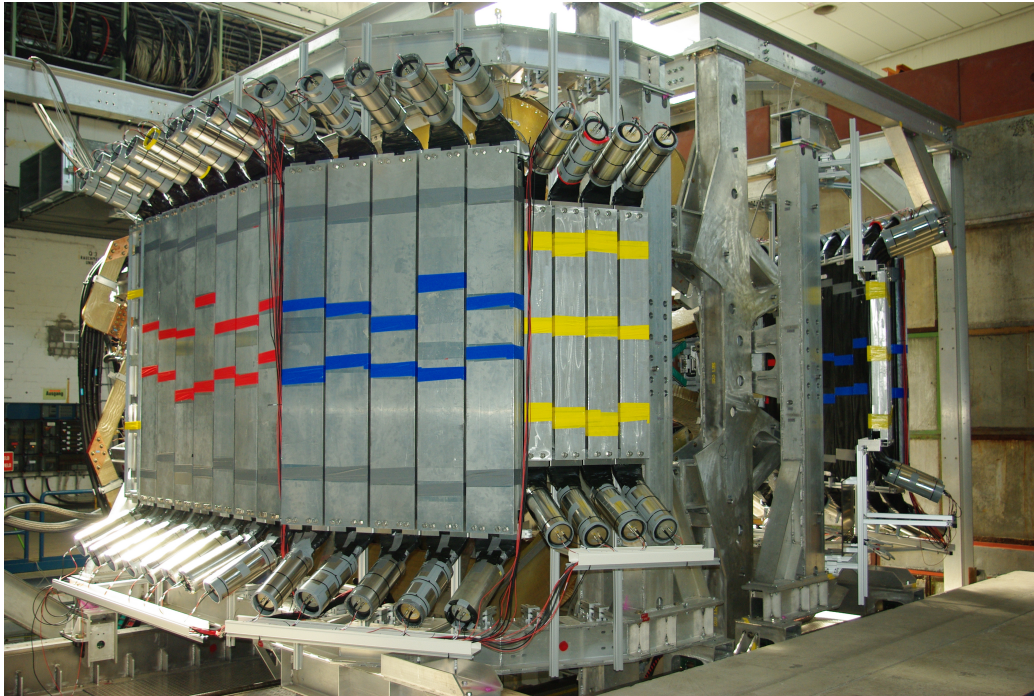


Fig. 16: Photograph of the mounted ToF detectors during OLYMPUS assembly of the OLYMPUS detector.

433 The main trigger logic of the experiment required presence of at least one
434 top/bottom ToF PMT coincidence in both sectors (see Sec. 6). The ToF
435 PMT signals were processed through passive splitters and recorded by both
436 TDCs and ADCs. The signals from the analog output were discriminated
437 with constant fraction discriminators (CFD) and the logic signals were fur-
438 ther processed for the trigger, to start the individual ToF TDC, and to gen-
439 erate the common stop signal for all TDCs. The rearmost two bars in each
440 sector were not present in BLAST, and were added to expand the acceptance
441 of OLYMPUS at large θ . Their signals were processed with leading-edge (LE)
442 discriminators. The differential splitter outputs were connected to the ADCs
443 for signal integration. The integrated ADC signal from a given bar pro-
444 vided an estimate of the energy deposited in the bar, while the relative time
445 difference between the top and bottom tube signals from a bar provided a
446 rough measurement of the hit position. The mean signal times of the top and
447 bottom signals were approximately independent of the hit position. Mean
448 times between pairs of ToF bars in both sectors provided measurements of
449 the time-of-flight of cosmic ray particles and of the difference in time-of-flight
450 between the scattered and recoiling particle from interactions in the target.

451 The active volume of the ToF bars consisted of Bicron⁷ BC-408 plastic
452 scintillator, chosen for its fast response time (0.9 ns rise time) and long
453 attenuation length (210 cm). At the ends of each bar, the sensitive volumes
454 were connected via Lucite light guides to 3-inch diameter Electron Tubes⁸
455 model 9822B02 photomultiplier tubes equipped with Electron Tubes EBA-01
456 bases. The PMT signals exhibited a typical amplitude of ~ 0.8 V with a rise
457 time of a few ns. The light guides were bent away from the interaction region
458 so as to orient the PMTs roughly perpendicular to the toroidal magnetic field.
459 Additionally, each PMT was encased with μ -metal shielding. Due to these
460 measures, the toroidal magnetic field had no discernible effect on the ToF
461 gains. Each PMT base utilized actively-stabilized voltage dividers to avoid
462 variation of signal timing with gain.

463 Due to aging and radiation damage of the bars, somewhat smaller atten-
464 uation lengths of 120-180 cm were found from the analysis of TDC and ADC
465 signals, shown in Fig. 17. Some of the bars showed advanced opaqueness and
466 were replaced before data taking. The level of degradation of the remaining

⁷Bicron, Solon, OH, USA

⁸Electron Tubes Ltd, Ruislip, Middlesex, England

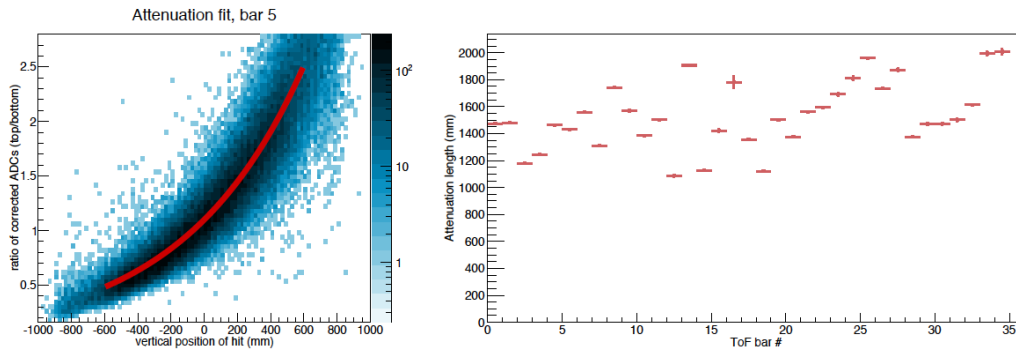


Fig. 17: A sample fit to the TDC and ADC data from a single bar to produce an estimate of the attenuation length for the bar (left) and the results of this fit for all bars (right).

467 bars was still tolerable and did not adversely affect the ToF performance.
 468 The efficiencies for top/bottom coincidences were measured by sandwiching
 469 each bar with a pair of small test scintillators and were found to be around
 470 98-99% for signals registered near the center of the bar. Additional ToF effi-
 471 ciency estimates were conducted by evaluating events with minimum trigger
 472 bias.

473 5. Luminosity Monitors

474 In order to measure the ratio of differential cross sections for positron-
475 proton and electron-proton elastic scattering, it was essential to monitor the
476 luminosity for each run very precisely. In particular, the physics goals of
477 OLYMPUS required the very precise and accurate measurement of the ratio
478 of the integrated luminosities with positron and electron beams delivered to
479 the experiment. OLYMPUS required a system in which individual measure-
480 ments of the instantaneous luminosity were made with sufficient statistical
481 precision and over sufficiently small times scales so as to eliminate effects
482 from any slowly varying parameters that affect the response of the detectors.
483 To achieve this, OLYMPUS included three systems to measure the luminosity
484 redundantly:

- 485 - The slow control system (Sec. 8) monitored the beam current and gas
486 flow to the target. The system additionally used measurements of the
487 target cell temperature, in conjunction with the known cell geometry,
488 to compute the target density and thickness during running. The prod-
489 uct of the target thickness and beam current integrated corrected for
490 the deadtime of the data acquisition system over a run produced an
491 approximate first estimate of the integrated luminosity of a data run.
- 492 - The 12° luminosity monitors (Sec. 5.1) measured elastically scattered
493 leptons over a small angular range around $\theta \approx 12^\circ$ in coincidence with
494 the recoil proton in the rear of the opposite sector drift chamber. Each
495 monitor consisted of a telescope of three triple gas electron multiplier
496 (GEM) detectors (Sec. 5.1.1) interleaved with three multi-wire propor-
497 tional chambers (MWPCs) (Sec. 5.1.2). Since at $\theta = 12^\circ$ the two-
498 photon contribution to elastic scattering is expected to be negligible,
499 the known ep elastic cross section at this angle can be used to provide
500 a beam species independent luminosity measurement. The 12° system
501 was designed to measure the luminosity with statistical precision better
502 than 1% per hour.
- 503 - A high precision measurement using symmetric Møller and Bhabha
504 scattering was implemented using PbF_2 calorimeters placed symmet-
505 rically at $\theta = 1.29^\circ$ in the left and right sectors (Sec. 5.2). Comparing
506 the observed e^-e^- and e^+e^- elastic scattering rates with the known
507 Møller and Bhabha cross sections provided a measure of the luminosity

508 for each beam species with the very high statistical precision in very
509 short time frames.

510 The implementations of the 12° and symmetric Møller/Bhabha luminos-
511 ity monitoring systems are discussed in detail in the immediately following
512 sections, while Fig. 18 provides a schematic overview of these systems.

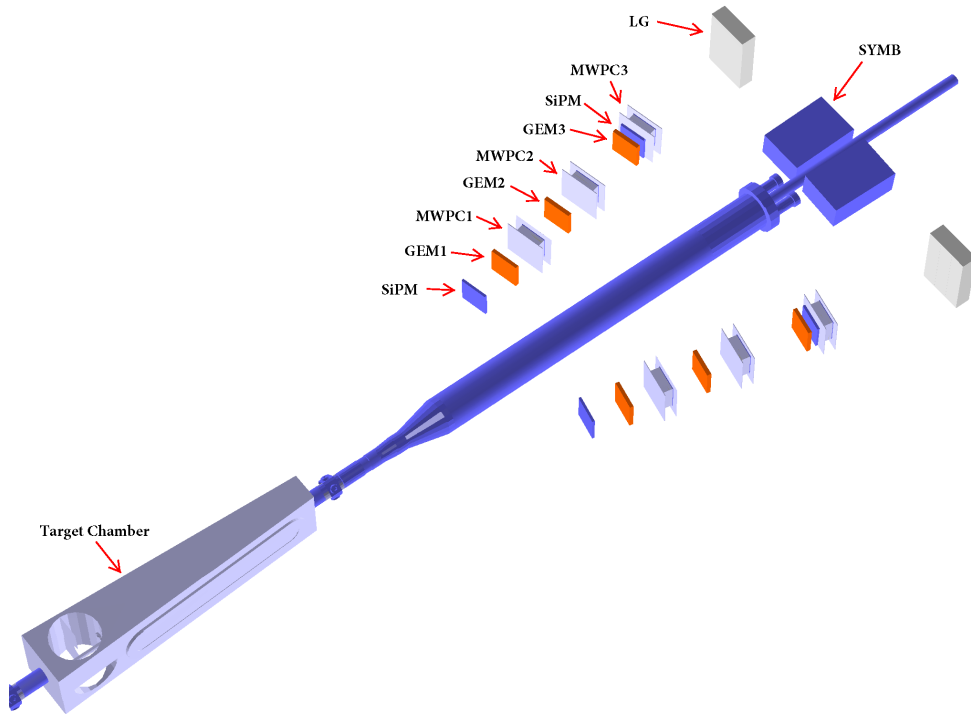


Fig. 18: Overview of the luminosity monitoring systems based on elastic ep scattering at $\theta = 12^\circ$ (GEM/MWPC) and symmetric Møller/Bhabha scattering (SYMB calorimeter).

513 *5.1. The 12° Luminosity Monitoring System*

514 The 12° luminosity monitoring system consisted of two telescopes each
515 composed of three triple-GEM and three MWPC elements, triggered by a
516 pair of thin scintillators with silicon photomultiplier (SiPM) readout. There
517 were several considerations which drove the design of the 12° system. The
518 detector elements were desired be low mass and with an active area of about
519 $10 \times 10 \text{ cm}^2$, corresponding to an approximate solid angle of 1.2 msr at a
520 maximum distance of about 2.9 m from the target. The detector acted as
521 a tracking telescope covering a range of the small lepton scattering angle
522 region where the asymmetry between electron and positron scattering was
523 expected to be negligible. The telescopes fit in the forward cones between
524 the pairs of toroid coils on each side of the beamline with a clear view of
525 the scattering chamber window and cell. While the telescopes were initially
526 designed with only the three GEM layers, the design for the MWPCs ul-
527 timately used was already available and was accommodated to provide an
528 additional independent monitor. A picture of such a telescope is shown in
529 Fig. 19.

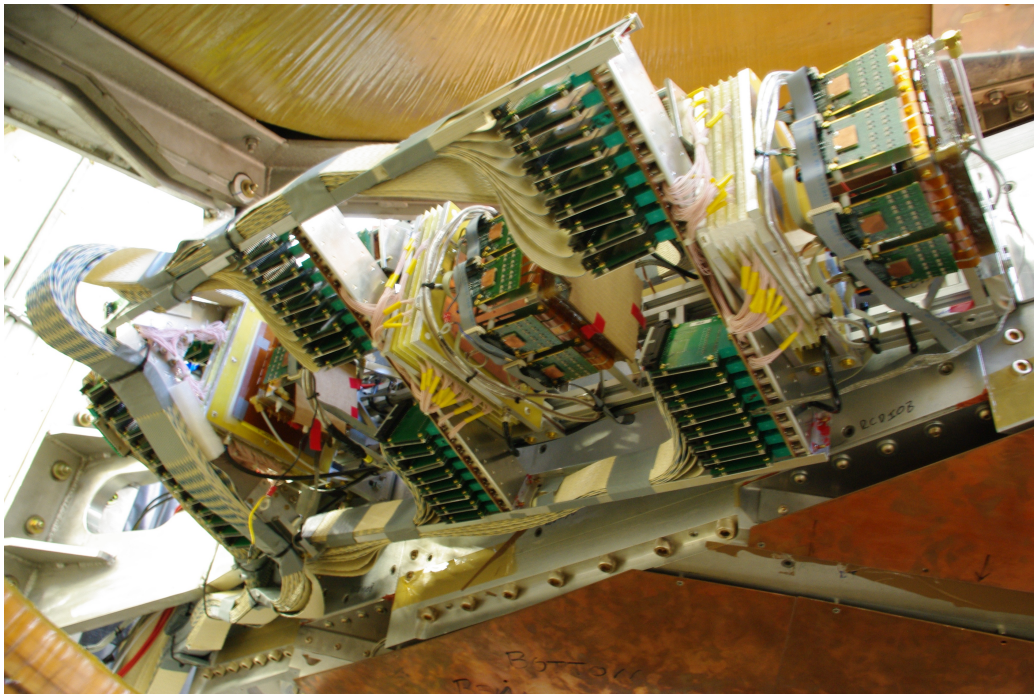


Fig. 19: Photograph of one of the 12° GEM/MWPC telescopes.

530 The readout for each telescope was triggered with pairs of thin scin-
531 tillators in each arm in coincidence with the signal from the recoil proton
532 registered in the rear ToFs of the opposite sector. With the chosen design,
533 the monitoring rate guaranteed a statistical precision better than 1% per
534 hour at the design luminosity of $2 \times 10^{33} \text{ cm}^{-2} \cdot \text{s}^{-1}$). The design was a trade-
535 off between the resolution and total detector acceptance and the smallness
536 of scattering angle in order to maximize the elastic count while minimizing
537 the possible asymmetry between e^+ and e^- scattering due to two photon
538 exchange.

539 5.1.1. 12° GEM Detectors

540 Six planar triple-GEM detectors with 2D strip readout were constructed
541 at Hampton University and installed in sets of three on either side of the
542 experiment to form telescopes aligned along $\theta = 12^\circ$ relative to the beamline.
543 The GEM detectors were designed at the MIT Bates Linear Accelerator
544 Center. Six GEM chambers were installed, interleaved with the 12° MWPCs
545 and trigger scintillators, and mounted on an integrated support structure
546 attached to the forward face of the large drift chambers.

547 The detector was designed to utilize front-end electronics and readout
548 cards designed and built by INFN Rome. MIT's experience designing and
549 constructing large area GEM detectors for the Forward GEM Tracker (FGT)
550 upgrade to STAR at RHIC (28) also provided design insight to make the
551 detector easy to construct and robust.

552 Each individual GEM chamber was constructed as a stack of frames and
553 foils glued together (see Fig. 20). Each stack included a readout board with
554 three GEM foils and a cathode foil above the active area. Two pressure
555 volume foils formed the outermost layers of the stack. There was a 2 mm
556 space between each GEM foil and between the last GEM foil and the readout
557 board. The pressure volume foils and the high voltage foils were spaced 3 mm
558 from the adjacent foils. All of the components were tested individually before
559 they were assembled into a detector. All of the electrical and gas connections
560 were accessible on the edges of the stack, or in special cut outs in the case of
561 the high voltage connections. A simple resistive voltage divider card provided
562 the high voltage to all foils. A standard non-flammable premixed gas of
563 Ar:CO₂ 70:30 was used for the detector volume.

564 The GEM foil, cathode, and readout foils were manufactured by TechEtch

565 Inc. in Plymouth, MA⁹. Each GEM foil consisted of 50 μm thick Kapton
566 clad on both sides with 5 μm thick layers of copper. The GEM foils were
567 perforated with 70 μm holes at a 140 μm pitch over the entire area of the
568 detector (approximately $10 \times 10 \text{ cm}^2$). A special cathode foil was made
569 of a piece of 50 μm Kapton layer with a 5 μm copper layer on only one
570 side and n holes to provide a uniform electric field throughout the primary
571 ionization area. Pressure volume foils on top of the cathode foil and below
572 the readout foil prevented the gas pressure inside the detector from deforming
573 the readout foil or the cathode foil. The pressure volume foils consisted of 50
574 μm thick aluminized Mylar, which additionally served to electrically shield
575 the detector. The readout foil consisted of a 50 μm thick Kapton substrate
576 foil. On the charge collection side of the foil there were precisely spaced
577 pads and lines of 0.5-1 oz. (18-35 μm) gold-plated copper. The lines aligned

⁹<http://www.tech-etech.com/>

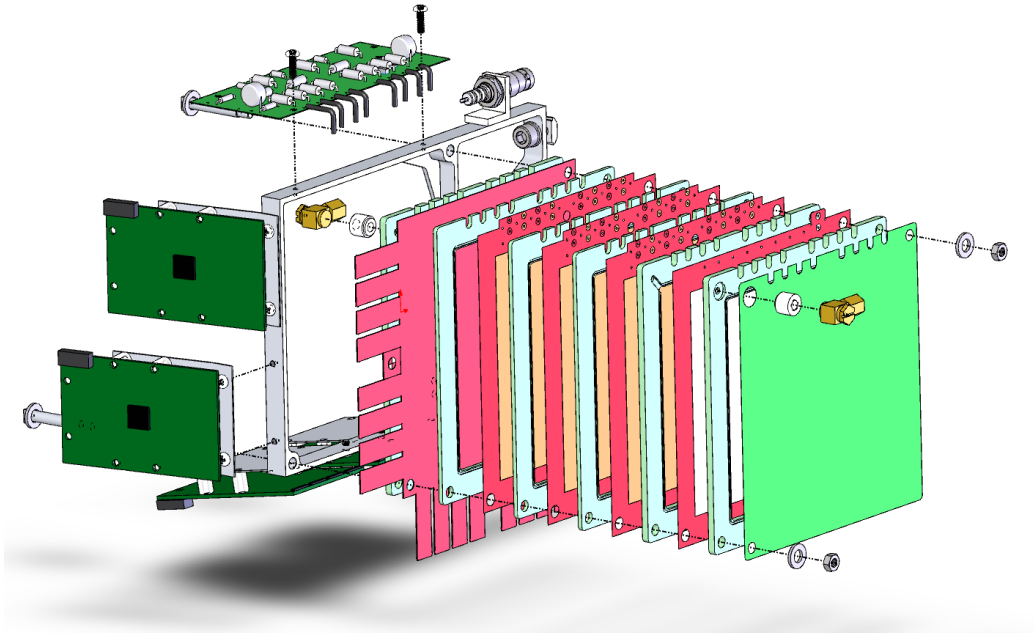


Fig. 20: An exploded view of a single triple-GEM detector.

578 vertically provided the horizontal coordinate of a hit. The pads were each
579 connected with a via to the backside of the foil where they were connected
580 to form rows to measure the vertical coordinate of a hit. The lines were
581 $124\ \mu\text{m}$ wide, at a $400\ \mu\text{m}$ pitch. The pads were $124 \times 323\ \mu\text{m}^2$, and also
582 arranged at a $400\ \mu\text{m}$ pitch. The spacing between the pads and the lines
583 was $76\ \mu\text{m}$, and $70\ \mu\text{m}$ between adjacent pads. The geometry was chosen
584 such that the charge collected with the readout layer would be approximately
585 equally shared between the horizontal and vertical readout channels.

586 The signals from the lines and pads were routed to two edges of the foil
587 where they terminated on sixteen small arrays of pads designed to fit a flexible
588 circuit connector, which was mounted on the front-end electronics card. Each
589 card had four connectors (two cards per coordinate) corresponding to a total
590 of four cards per GEM detector. Each GEM detector had 500 channels (250
591 per coordinate), with a total of 3000 readout channels for the GEMs in both
592 telescopes. The front-end readout card designed by INFN Rome used one
593 APV25-S1 analog pipeline chip per card (29). Each chip had 128 channels,
594 each of which had a 192 cell analog pipeline which sampled the input channels
595 at 40 MHz. Data were read out of the pipeline after a trigger event. All 128
596 channels were multiplexed onto a single data line which then ran to the DAQ
597 system. The communication between the APV card and the DAQ system was
598 maintained by a VME based control module hosting a field-programmable
599 gate array (FPGA).

600 The finished detectors were mounted on an aluminum mounting bracket
601 attached to the mounting rails that also held the MWPCs. The mounting
602 bracket had flexible supports for the high voltage card and for the front
603 end electronics cards. These allowed the positions of the cards to be ad-
604 justed during installation to avoid interference between components. Both
605 the mounting bracket and the mounting rails were adjustable. Fiducials lo-
606 cated on the GEM chambers allowed for precise surveying of the detector
607 positions after the mounting was adjusted.

608 A charged particle traversing the GEM elements produced a charge clus-
609 ter which was registered by several strips in both the vertical and horizontal
610 directions. The reconstructed location of the clusters in x and y gave the
611 spatial location of the particle as it passed through the detector. Digitization
612 of the signal amplitudes of all channels allowed the detector to achieve high
613 spatial resolution using centroid analysis. Intrinsic resolutions of approxi-
614 mately $70\ \mu\text{m}$ have been achieved. The efficiency of each GEM detector was
615 measured with candidate tracks based on the other five telescope elements

⁶¹⁶ and were found to be around 95% for all GEM elements.

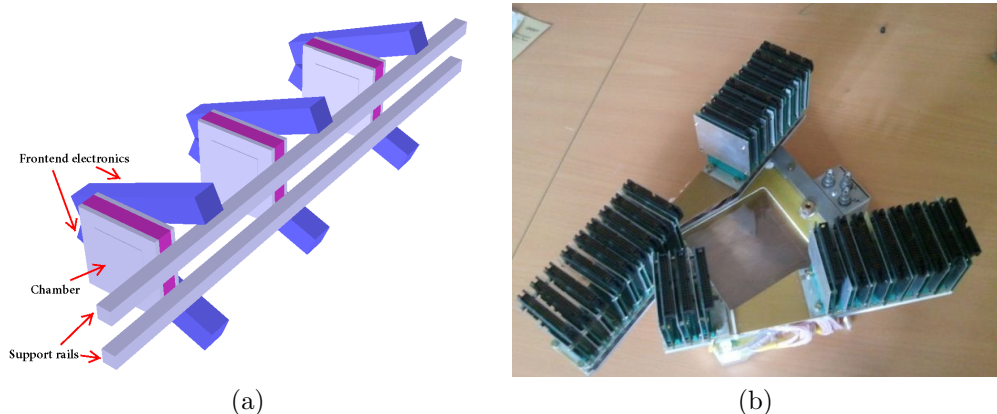


Fig. 21: (a) Three MWPC modules, including their CROS3 readout electronics, were deployed in each 12° telescope arm. (The GEM detectors and trigger scintillation counters are not shown. (b) Photograph of one MWPC with CROS3 readout electronics

617 *5.1.2. 12° Multi-Wire Proportional Chambers*

618 Six identical MWPC modules, along with their CROS3 readout electronics (30), were fabricated at PNPI for the 12° luminosity telescopes. Three
 619 MWPCs were deployed in each telescope arm, as shown in Fig. 18. The
 620 readout cards for each module were arranged in two stacks around the active
 621 area, and are shown in Fig. 21. The stacks were angled so that they could
 622 fit in the narrow space between the coils of the toroid.
 623

624 Each MWPC module consisted of three planes of anode sense wires inter-
 625 leaved with cathode wire planes. The sense wires were made of gold-plated
 626 tungsten, had a diameter of $25\ \mu\text{m}$, and 1 mm separation. The cathode wires
 627 were made of beryllium bronze, with a diameter of $90\ \mu\text{m}$, and a separation
 628 of 0.5 mm. Each plane of wires had its own fiberglass frame. The module
 629 was assembled by sandwiching the planes together in a 10 mm aluminum
 630 outer frame. The three anode planes, labelled X, U, and V, had different
 631 orientations in order to measure a two-dimensional hit position. The U and
 632 V planes were angled by $\pm 30^\circ$ relative to the X plane, whose wires were
 633 vertical. Various parameters for the MWPCs are presented in Table 1.

634 A gas mixture of $65\%\text{Ar}+30\%\text{CO}_2+5\%\text{CF}_4$ was chosen for the MWPCs
 635 based on the experience gained from the proportional chambers produced at
 636 PNPI for the HERMES Experiment (31). According to calculations using
 637 the program GARFIELD (32), this mixture would produce a gas gain of

Active area	$112 \times 112 \text{ mm}^2$
External dimensions	$180 \times 180 \times 50 \text{ mm}^3$
Anode planes	X (0°), U ($+30^\circ$) and V (-30°)
Gap between anode and cathode	L=2.5 mm
Sense wire spacing	S=1 mm
Cathode wire spacing	$S_{cath}=0.5 \text{ mm}$
Sense wire diameter	D=0.025 mm Au-plated tungsten
Cathode wire diameter	$D_{cath}=0.090 \text{ mm}$ beryllium bronze
U, V angle wrt X wire	$\pm 30^\circ$
MWPC material in acceptance	$\sim 0.25\%$
Working gas mixture	65%Ar+30%CO ₂ +5%CF ₄
Gas gain at work point	$\sim 7 \times 10^4$

Table 1: Working parameters of the MWPC modules

638 7×10^4 in the MWPCs at the preliminary operating voltage of 3150 V. The
639 operating voltage was chosen to be 3200 V after testing the MWPCs with a
640 ^{55}Fe radioactive source. The results of this study are shown in Fig. 22. This
641 operating voltage was validated by efficiency measurements during running
642 conditions, where an efficiency of 98–99% was typically seen for all MWPC
643 modules. Hit distributions for each plane, taken during the experiment are
644 presented in Fig. 23.

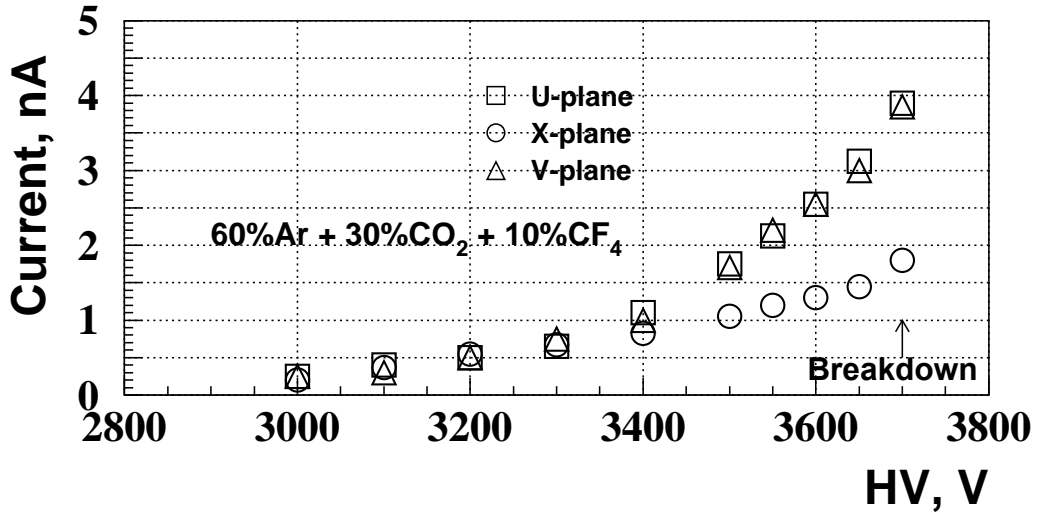


Fig. 22: Measured current on one MWPC from a ^{55}Fe radioactive source

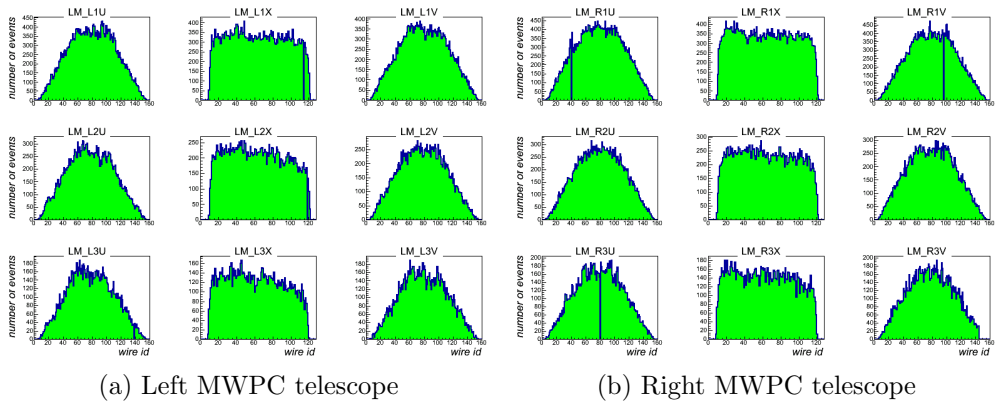


Fig. 23: Hit distributions for the left and right MWPC telescopes showing the XUV planes for the three detectors; one can see that just a few channels were lost because of the contact imperfections in the cards' connectors.

645 *5.1.3. 12° Trigger*

646 Each 12° telescope included two $120 \times 120 \times 4$ mm³ scintillator tiles (El-
647 jen EJ-204) to provide a trigger signal for the GEMs and MWPCs. Each
648 scintillator tile was wrapped in Millipore Immobilon-P diffuse reflectors and
649 read-out using two Hamamatsu multi-pixel silicon photomultipliers (MPPC)
650 mounted on opposite corners of the tiles. This ensured a very high homogene-
651 ity of the light yield from the entire area of the tiles. The analog signals from
652 each MPPC were summed and constant fraction discriminators provided the
653 output signal from each tile. The trigger for reading out the 12° telescope
654 on a given side consisted of the triple coincidence of the the two tiles on that
655 side in conjunction with a trigger from a ToF bar in the rear region of the
656 opposite side of the detector.

657 Additionally, lead glass calorimeters mounted behind the 12° telescopes in
658 each section provided an independent means of triggering the detectors. Each
659 calorimeter consisted of three lead glass bars attached to a PMT for readout.
660 The additional trigger contributed the ability to measure the efficiency of
661 the tile trigger continuously throughout data taking. The scintillator tiles
662 exhibited efficiencies well in excess of 99% throughout the entirety of the
663 experimental run.

664 5.2. Symmetric Møller/Bhabha Luminosity Monitor

665 The symmetric Møller/Bhabha scattering luminosity monitor (SYMB)
 666 monitored the luminosity delivered to the OLYMPUS experiment by mea-
 667 suring symmetric lepton-lepton scattering from the target. The scattering
 668 processes monitored consisted of Møller scattering ($e^-e^- \rightarrow e^-e^-$) in the
 669 case of electron beam running and Bhabha scattering plus annihilation to
 670 two photons ($e^+e^- \rightarrow e^+e^-$ and $e^+e^- \rightarrow \gamma\gamma$) in the case of positron beam
 671 running. At the OLYMPUS beam energy of 2.01 GeV, symmetric scattering
 672 occurred at a polar angle of 1.298° with respect to the beam direction (see
 673 Fig. 24).

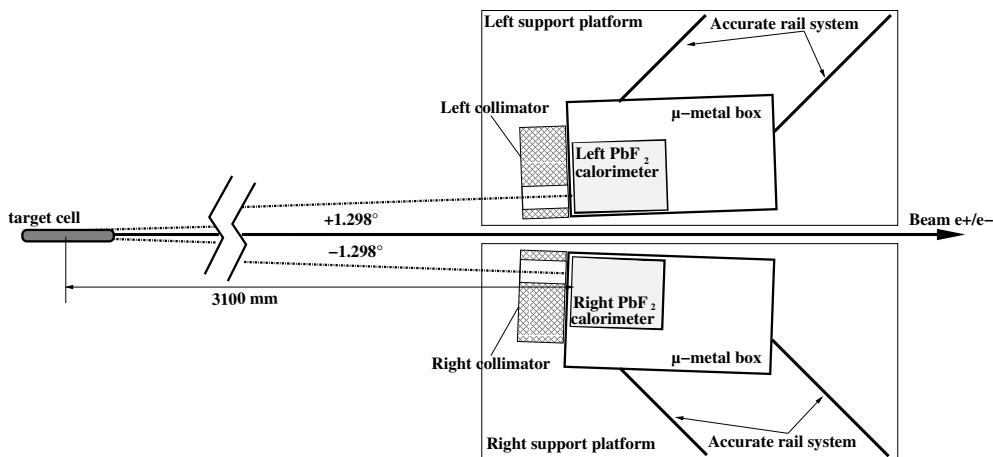


Fig. 24: A schematic of the Symmetric Møller/Bhabha luminosity detector (SYMB) showing the symmetric design about the beamline.

674 The detector provided a means measuring the luminosity with high pre-
 675 cision by using the fact the cross sections for the monitored processes are
 676 very high in the forward direction and are precisely calculable from quan-
 677 tum electrodynamics. The identification of the symmetric coincidence of the
 678 decay products in combination with the very high statistics of the measure-
 679 ment provided a means of determining the relative luminosity of electrons
 680 and positrons delivered to the experiment with the necessary precision for
 681 the OLYMPUS physics goals.

682 The SYMB, constructed at Johannes Gutenberg Universität in Mainz,
 683 Germany, consisted of two symmetric 3×3 arrays of lead fluoride (PbF_2)

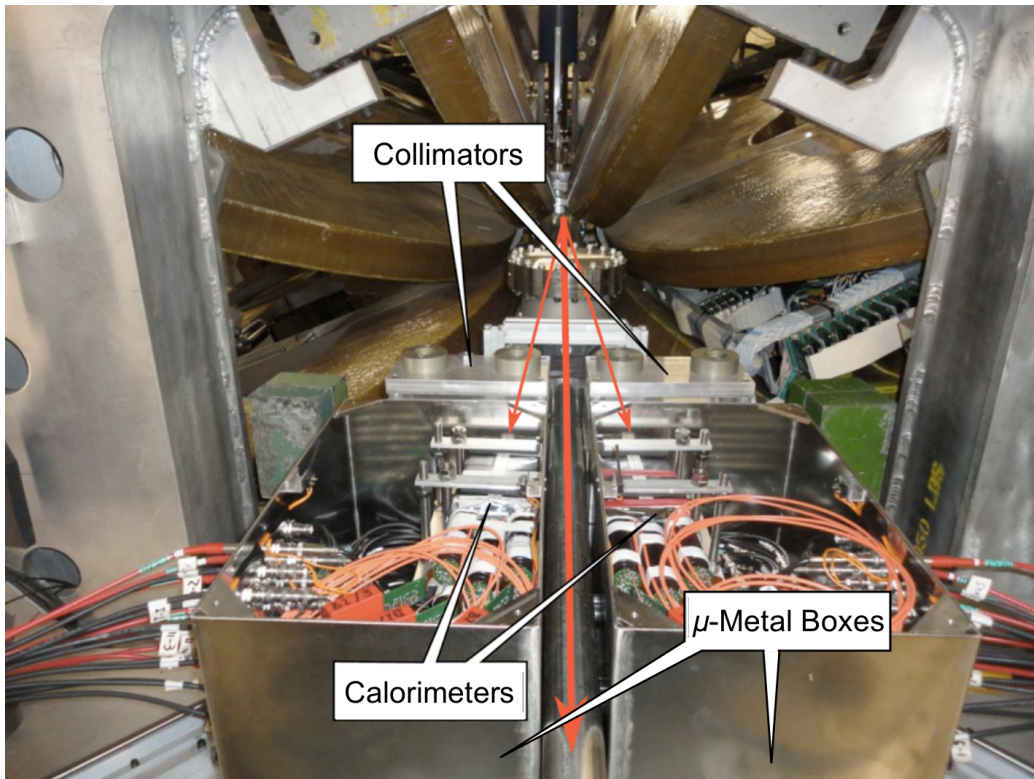


Fig. 25: A photograph showing the main components of the SYMB detector. The thick red line indicates the direction of the beam while the thinner red lines indicate the general path of scattered electrons and positrons entering the SYMB.

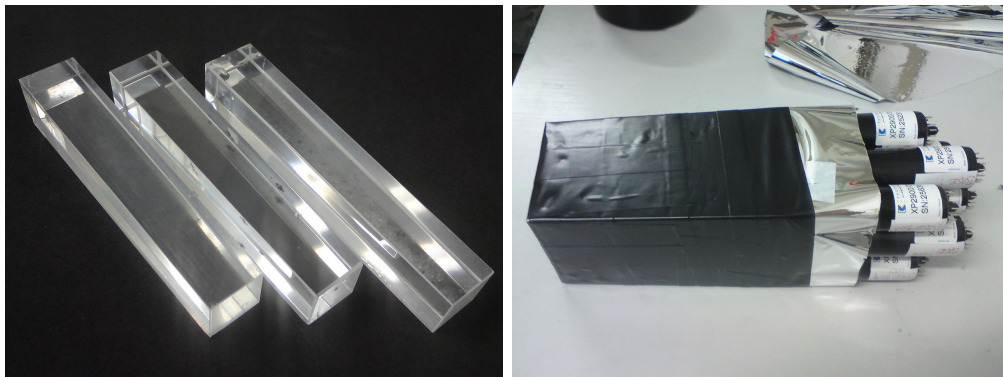


Fig. 26: Several of the PbF_2 crystals used in symmetric Møller/Bhabha luminosity monitor before (left) and after (right) assembly with the PMT readout system.

684 crystals, as shown in Fig. 26. A Philips XP 29000/01 PMT connected to
685 the end of each crystal to provide readout. Each crystal was approximately
686 26 mm×26 mm×160 mm, with a slightly tapered shape. The array of crystals
687 on each side corresponded to approximately 17 radiation lengths and
688 2.17 Molière radii of PbF₂, which allowed containment of 98.9% of the trans-
689 verse electromagnetic showers associated with the events of interest within
690 a compact volume. Additionally, the SYMB successfully operated at the ex-
691 tremely high rates in the small angle region by combining very fast response
692 PMTs (20 ns) with the fact that particles in PbF₂ produce only Cherenkov
693 radiation, which eliminates the delay associated with a scintillation signal.
694 Millipore paper wrapping around each crystal increased the surface reflectiv-
695 ity to reduce light loss and each detector resided inside a μ -metal to shield
696 the device from the magnetic fields of the OLYMPUS toroid and the DORIS
697 beamline.

698 Lead collimators, located between each detector array and the target,
699 shielded the crystals from beam bremsstrahlung, non-symmetric Møller/Bhabha
700 events, and other backgrounds. Each collimator consisted of a 100 mm thick
701 lead block with a precision- machined circular hole with diameter 20.5 mm.
702 Since these apertures determined the solid angle acceptance of each detector,
703 the location and orientation of the collimator holes was carefully surveyed
704 before and after each running period.

705 *5.2.1. Readout Electronics*

706 The SYMB readout electronics were based on a designed used for the A4
707 Experiment at MAMI in Mainz (33). The system provided the ability to
708 conduct fast analog summation of the 9 PMT signals from each crystal and
709 to quickly digitize and histogram the summed signal. The detector operated
710 at and digitally histogrammed events up to a rate of 50 MHz (limited by the
711 20 ns signal time of the PMTs). Typical single event rates in the detectors
712 during DORIS operation were 10 MHz, well within the operational capability
713 of the device.

714 Fig. 27 shows a schematic of the readout system. First, the system
715 summed the 9 analog signals from the crystal array and split this signal into
716 three channels for the coincidence, master, and slave modes. Simultaneous
717 with the summing (to accommodate the high event rate), the signals from
718 the nine crystals were compared to determine if the center of the EM shower
719 occurred in the center crystal to reject noise events. When this condition
720 was satisfied in conjunction with the summed signal exceeding the threshold

721 of a constant fraction discriminator the system generated a trigger signal for
 722 the digital histogram system. Due to the high event rate, no single events
 723 were read-out.

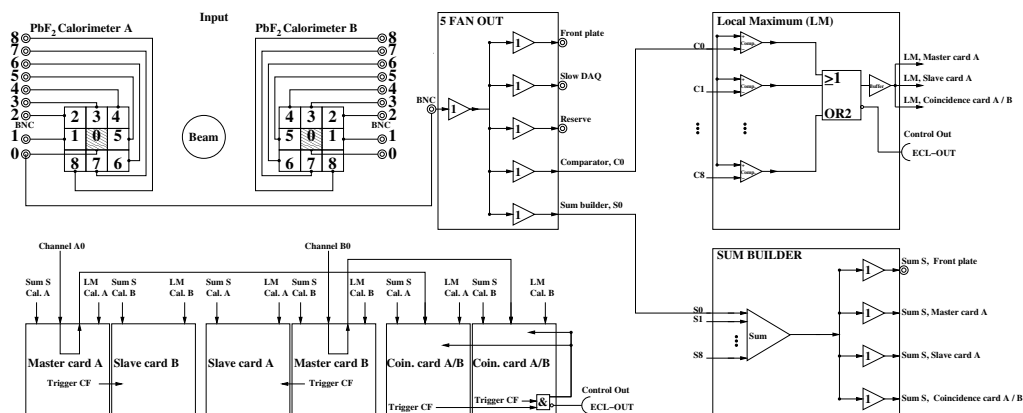


Fig. 27: A schematic of the signal flow through the SYMB data acquisition electronics.

724 5.2.2. Event Selection

725 Event selection for the SYMB detector utilized the fact that symmetric
 726 Møller, Bhabha, and annihilation events exhibited equal energy deposition
 727 in both calorimeters, while many background processes deposited energy
 728 asymmetrically. The detector generated three histograms from the recorded
 729 events. The coincidence mode required the signal from both sides to exceed
 730 the discriminator threshold, while the other two modes independently recorded
 731 single arm events over threshold. Fig. 28 shows an example of the
 732 coincidence event histogramming.

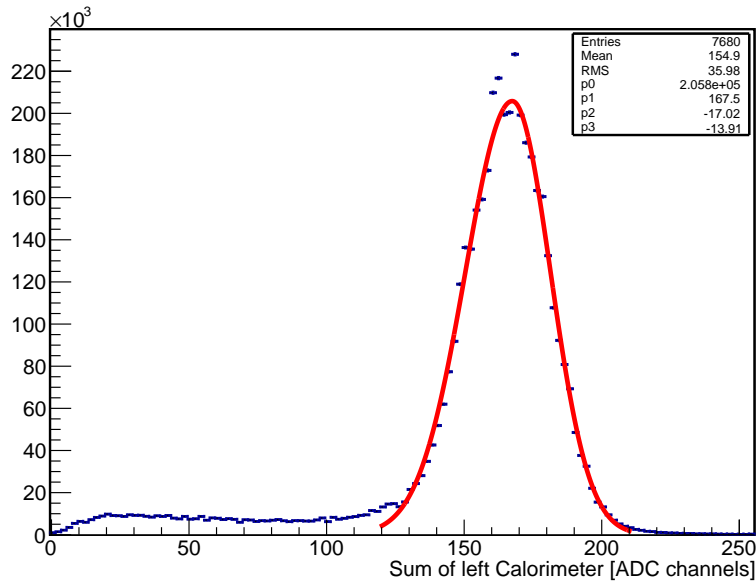
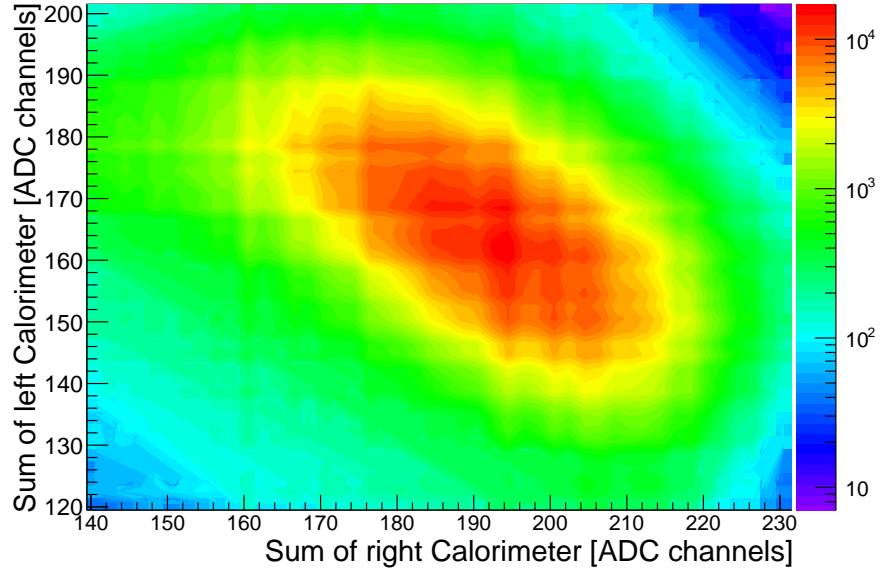


Fig. 28: Top: A 2D histogram of the sum of the deposited energy in the left and right SYMB calorimeters in coincidence mode. Bottom: A projection of the sum of the deposited energy in the left calorimeter, corrected for the differential non-linearity of the ADC.

733 6. Trigger

734 The OLYMPUS Experiment required the development of a new trigger
735 system that incorporated information from the reused detector components
736 from BLAST, the new luminosity detectors, as well as information from the
737 DORIS accelerator. This was implemented using a VME field programmable
738 gate array (FPGA), which allowed the combination of up to 16 input signals
739 from various systems to produce 16 parallel trigger conditions, which could
740 be prescaled to control the rate at which different conditions were recorded.

741 The ToF scintillator bars and the SiPMs in the 12° luminosity monitors
742 provided the fast trigger signals for the experiment, while the DORIS accel-
743 erator provided timing information. The primary trigger signal consisted of
744 requiring coincidence between the top and bottom PMTs of a ToF bar in
745 both the left and right sectors of the detector. The ToFs were grouped such
746 that the trigger signal was produced only when the relative position of the
747 left and right bars corresponded to the expected kinematics of an elastic $e^\pm p$
748 event. The main 12° luminosity trigger consisted of a coincidence between
749 the two SiPMs in one sector and a ToF in the opposite sector. The DORIS
750 bunch clock was used provided the reference time signal for the ToF and drift
751 chamber TDCs.

752 In addition to the primary triggers, several signals corresponding to less
753 strict ToF coincidences and signals from the lead glass calorimeters behind
754 the 12° were included at higher prescale factors. Events from these trig-
755 gers provided means of monitoring the efficiencies and calibration of various
756 detector components over the course of data-taking.

757 During the February data run, inspection of the collected data indicated
758 that the number of elastic $e^\pm p$ events in the recorded data was an unsatis-
759 factorily small fraction of the number of triggers. To improve this for the
760 Fall run, a second-level trigger was implemented to incorporate data from
761 the drift chambers. The TDC signals from the drift chamber sense wires in
762 the middle and outer chambers in each side were grouped so as to produce a
763 second-level trigger signal only when at least one wire in each of the middle
764 and outer chambers on each side. This signal was combined with the primary
765 ToF trigger to form the main trigger signal for the Fall run. This scheme
766 succeeded in reducing the false trigger rate by a factor of approximately
767 10, which was critical to controlling the trigger rate during high luminosity
768 “top-up” running (see Sec. 9).

769 7. Data Acquisition System

770 The OLYMPUS data acquisition system (DAQ) utilized the framework
771 originally developed for the Crystal Barrel Experiment at ELSA accelerator
772 in Bonn, Germany. The implementation and hardware for the DAQ was
773 provided by the Bonn group. The system was “synchronous” in that each
774 detector was read-out simultaneously upon a common event signal, which
775 ensured the event-by-event coherence of the data collected. While this ap-
776 proach significantly increased the complexity of the DAQ in comparison to
777 a free-running system, reading the detector components synchronously con-
778 ferred a number of advantages such as the ability to immediately identify
779 readout errors from individual channels, definitive matching of data from
780 different systems corresponding to the same event, and an overall increase in
781 reliability of the system. Additionally, the system provided a graphical user
782 interface for the control of data-taking and an integrated run database that
783 was available via a web interface.

784 Synchronous operation was achieved via a master-slave hardware system.
785 A schematic of the system is shown in Fig. 29. The system consisted of
786 a number of 6U VME-Modules, one of which served as the *master*. The
787 *master* module was responsible for monitoring the state of each of the *client*
788 modules, each of which handled the signals from a set of detector elements.
789 Each module contained a VME CPU for handling of the data readout. During
790 data taking, each of the *client* modules signaled its state to the *master* via
791 its “Busy+Okay” lines. The *master* generated an event trigger signal and
792 distributed it to the clients only when all clients reported that they were
793 functioning.

794 The signal sequence for the generation of a synchronous event signal by
795 the DAQ is shown in Fig. 30. The *master* first sent an event request to the
796 *client* modules, which responded by beginning the read-out of their detectors
797 and reporting “busy” to the *master*. Upon completion of its readout, each
798 *client* reported “Okay” to the *master*. Once all modules reported a successful
799 readout, the *master* generated an event trigger signal.

800 Each of the VME CPUs associated with a *client* module corresponded
801 to a specific subdetector (with some subdetectors requiring multiple CPUs)
802 and served as a “local event builder” (LEVB) for that subdetector. The
803 CPU associated with the *master* module served as the global event builder,
804 in that it collected data from each of the LEVBs and checked the results
805 for completeness before committing the data to disk. Communication be-

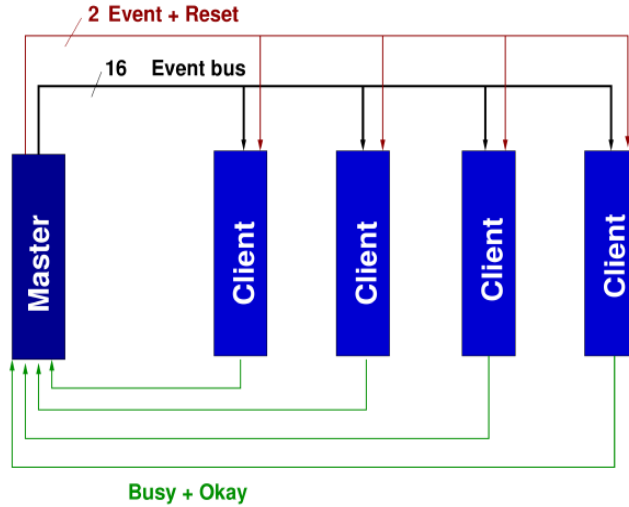


Fig. 29: Schematic of the master-slave layout of the DAQ synchronization system.

806 tween the global and local event builders was conducted over two dedicated
 807 1 GBit TCP/IP networks, which allowed the separation of data transfer sig-
 808 nals from control signals to minimize competition for bandwidth. Each of
 809 the LEVBs ran appropriate functions for interaction with the TDC, ADC,
 810 and/or scalar modules of its subdetector. The modular design of the DAQ
 811 system allowed for the construction of a synchronous readout system without
 812 excessive development time or manpower.

813 The global event builder featured a interchangeable output system en-
 814 abling a wide variety of data formats, which provided flexibility in choosing
 815 the the optimal data format for OLYMPUS. The global event builder could
 816 achieve an output event rate of 30 kHz, which was well above the limit im-
 817 posed by other elements of the detector.

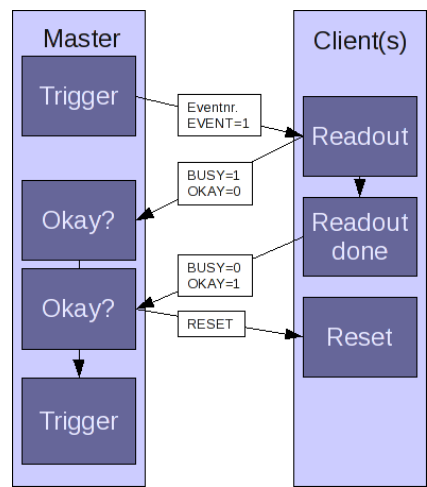


Fig. 30: Signal flow chart for the generation of an event signal in the synchronization system.

818 8. Slow Control

819 The operation of the OLYMPUS Experiment required the monitoring and
820 control of as well as the recording of data from several hundred devices in
821 various components of the detector and supporting systems. These devices
822 included high voltage supplies, vacuum pumps and gauges, the hydrogen
823 gas supply system, the parameters of the DORIS beam, and other elements
824 with operational time scales longer than that of the trigger. To satisfy these
825 requirements, a new dedicated slow control system was developed for OLYM-
826 PUS.

827 The slow control system utilized the Experimental Physics and Industrial
828 Control System (EPICS)¹⁰ as its backend solution. The system ran on three
829 Linux machines: two VME computers with interface cards connecting to the
830 control equipment and one server which communicated data to a PostgreSQL
831 database and interfaced with the DORIS control system. The databased
832 recorded the status and history of all parameters associated with the slow
833 control. The slow control also passed this data to the DAQ for integration
834 with the detector data to produce the run data files.

835 The slow control system included a user-friendly, web-accessible graph-
836 ical user interface, implemented using Flask as middleware. While typical
837 slow control systems require the deployment of custom, operating system
838 dependent software on their control computers, the design of the OLYMPUS
839 system allowed both view-only and control access from any computer with an
840 Internet connection. The user interface provided simple on-screen controls
841 for the various elements connected to the system, displayed real-time plots
842 and indicators of system statuses and data, and produced visual and audible
843 alarms when parameters failed to satisfy proper run conditions.

¹⁰<http://www.aps.anl.gov/epics/index.php>

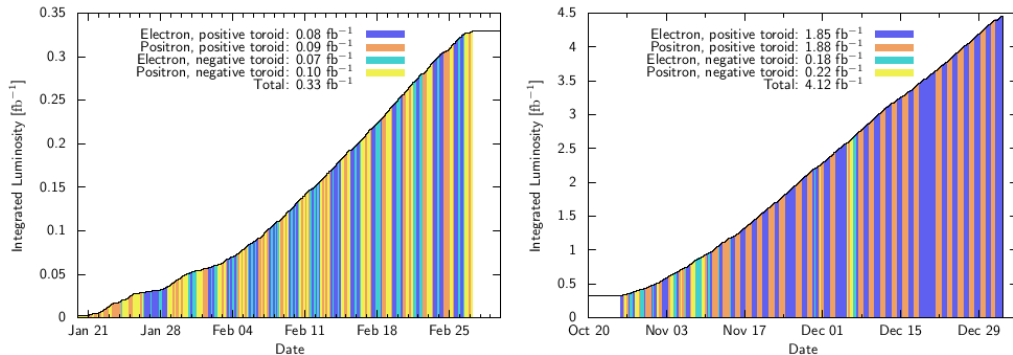


Fig. 31: The approximate integrated luminosity delivered to the OLYMPUS Experiment during the February (left) and fall (right) runs, as measured by the slow control (accurate to $\sim 10\%$).

844 9. Operation

845 During normal data-taking runs, a two-person shift crew operated the
 846 OLYMPUS detector and monitored the quality of the data using a number
 847 of plots generated in near real-time. Typically, production runs were taken
 848 24 hours a day during the February and fall runs, alternating daily between
 849 positron and electrons beams. The integrated luminosity delivered to the
 850 experiment during the two runs is shown in Fig. 31. In total, a data set
 851 of approximately 4.5 fb^{-1} was collected over the course of both runs. As
 852 discussed in Sec. 1, density of gas in the target cell during the February run
 853 was significantly lower than the design value due to a leak in the interface
 854 between the H_2 gas feed system and the target cell. Due to this, less than
 855 10% of the ultimate data set was collected during the February run. As is
 856 described in the following section, it was possible to run at higher average
 857 beam current during the fall run, which allowed the experiment to reach its
 858 initial integrated luminosity goals. At such higher currents, however, it was
 859 only possible to operate the experiment using a single toroid polarity (posi-
 860 tive) due to the fact that low energy electrons were bent into the detectors
 861 in the negative polarity, resulting in an inoperable background level. Uptime
 862 during the data-taking runs was extremely high (approximately 95%), with
 863 most of the downtime accounted for by the time required (on the order of an
 864 hour) to switch the beam species daily.

865 *9.1. Data Collection*

866 As previously noted in Sec. 2, the experiment employed two modes of
867 operation, differentiated by the manner in which the DORIS beam was oper-
868 ated. During the February run, the experiment was operated in “manual”
869 mode in which the beam was initially filled to ~ 65 mA and then data was
870 taken as the beam decayed to ~ 40 mA. At this point, the shift crew used
871 the slow control interface (Sec. 8) to lower the high voltage of the various
872 detectors to preset safe values. Since beam refills during the earlier running
873 period were not as clean as during the Fall 2012 run (more instability and
874 losses), the lowering of the voltages prevented high voltage trips and possible
875 damage to the detectors during the refill. After lowering the voltages, the
876 OLYMPUS shift crew informed the DORIS accelerator crew that the detec-
877 tor was ready for beam refill. Once the beam was restored to the normal
878 starting current, the voltages were brought back to operational values and
879 data-taking was restarted.

880 Between the February and fall runs, significant improvements were made
881 to the DORIS beam injection process that allowed the OLYMPUS Experi-
882 ment to be run in “top-up mode.” In this mode, the beam was initially filled
883 to ~ 65 mA as in the manual mode, but was only allowed to decay to ~ 58 mA
884 before triggering an automatic refill. Due to the improved injection, it was
885 not necessary to lower the high voltage of the OLYMPUS detectors during
886 these injections. The DAQ was configured to briefly inhibit data-taking dur-
887 ing injection pulses (see Sec. 2). This mode of running significantly increased
888 the average instantaneous luminosity delivered to the experiment and freed
889 the OLYMPUS shift crew to more carefully monitor the quality of the beam
890 and incoming data.

891 Due to the importance of collecting data with both positrons and elec-
892 trons, the beam species was switched each morning (with occasional excep-
893 tions for maintenance, balancing the amount of data collected with each
894 species, etc.). This ensured that there were no systematic differences be-
895 tween e^+ and e^- runs introduced by environmental factors such as day/night
896 cycles, reduced traffic on the DESY campus on weekends, etc. Similarly, dur-
897 ing the February run, in which both toroid polarities were used, data-taking
898 was segmented into four six-hour blocks each day. The pattern of toroid po-
899 larities in the four blocks each days was selected by coin toss to ensure equal
900 running time for each polarity while avoiding systematic effects due to the
901 time of day and week.

902 In addition to production runs, empty target runs (with the H₂ gas flow
903 shut-off and the target chamber pumped down to ring vacuum levels), zero
904 magnetic field runs, and other test runs were taken on an approximately daily
905 basis for the purposes of monitoring backgrounds, providing data for detector
906 calibrations, and testing proposed changes to operations. When the DORIS
907 beam was unavailable due to problems or maintenance, the detector was left
908 active to collect cosmic ray data. Also, cosmic ray data were collected for
909 approximately one month following the end of OLYMPUS productions runs
910 in January 2013. This large cosmic data set is being used for various studies
911 of detector efficiencies and for calibration.

912 *9.2. Data Quality Monitoring*

913 During data-taking, the quality of the incoming data was monitored in
914 several stages. Real-time, online monitoring of essential parameters was im-
915 plemented using the ExPIORA framework originally developed by the Crystal
916 Barrel collaboration (34). The ExPIORA program processed the raw data
917 ZEBRA files during data collection to produce a variety of histograms and
918 plot of quantities versus time, such as the number of drift chamber wires hit
919 per event, ADC and TDC distributions, DAQ deadtime, and various detector
920 rates. The OLYMPUS shift crew had access to reference plots corresponding
921 to those shown in ExPIORA that showed data of known good quality and
922 data representing known possible issues. This provided the shift crew with
923 the ability to quickly identify problems with detectors as well as problems
924 caused by poor beam quality and take action to resolve them rather than
925 taking low-quality data.

926 For the fall run, a second level of data quality monitoring by the shift crew
927 was implemented that allowed inspection of the data in a more processed for-
928 mat approximately 30 minutes after the conclusion of a single data run. This
929 program automatically ran basic analysis programs on complete datasets as
930 they became available and presented the data to the shift crew. In a similar
931 fashion as the real-time monitoring, this program presented histograms and
932 plots of the recent data to be compared with data of known quality, but
933 included higher-level information such as the properties of events with good
934 particle track candidates and basic measures of detector efficiencies.

935 Additionally, the long-term performance of the detector was monitored
936 using the slow control database discussed in Sec. 8. This provided the ability
937 to monitor the behavior of many detector parameters over the course of the

⁹³⁸ entire data-taking period to identify slow drifts and sudden changes that
⁹³⁹ could affect the analysis.

940 **10. Summary**

941 In 2012 the OLYMPUS experiment successfully collected approximately
942 4.4 fb^{-1} of data for electron and positron elastic scattering from hydrogen
943 at the DORIS storage ring at DESY. The experiment used a large accep-
944 tance, left/right symmetric detector system consisting a toroidal magnetic
945 spectrometer with drift chambers for tracking, time-of-flight scintillators for
946 triggering and relative timing, and a redundant set of luminosity monitors.
947 A flexible trigger and data acquisition system was used to collect the data.
948 The left/right symmetric design of the detector and the daily alternation of
949 beam species minimized the systematic uncertainties of the measurement.
950 The initial plan to additionally change the toroidal magnet polarity regu-
951 larly was not possible due to high background rates in the negative polarity
952 configuration. Consequently the majority (78%) of the data were collected
953 with positive magnet polarity.

954 This paper has provided a technical description of the accelerator, in-
955 ternal target, detector, electronics, and operation of the OLYMPUS exper-
956 iment. Future papers will detail the performance of the detector, analysis,
957 and physics results obtained.

958 **11. Acknowledgments**

959 The successful design, construction, and operation of the OLYMPUS Ex-
960 periment would not have been possible without the research and technical
961 support staffs of all of the institutions involved. In particular, we would like
962 to acknowledge the DORIS accelerator group for providing the high quality
963 electron and positron beams delivered to the experiment. We also gratefully
964 acknowledge the DESY MEA and MKK groups for providing the necessary
965 infrastructure and support during the assembly, commissioning, operation,
966 and disassembly of the experiment. The research and engineering group from
967 MIT-Bates was invaluable in all phases of the experiment, from disassembling
968 BLAST and shipping components to DESY and overcoming numerous unan-
969 ticipated problems during the installation of the experiment, particularly
970 with the target and vacuum systems.

971 We would like to thank E. Steffens for numerous suggestions and helpful
972 discussions during the initial development of the experiment.

973 Finally, we gratefully acknowledge the DESY directorate, particularly
974 Prof. Heuer and Prof. Mnich, and the DESY Physics Review Committee for
975 their support, advice, and encouragement from the start of the proposal.

976 This work was supported by the US Department of Energy and the Min-
977 istry of Education and Science of the Russian Federation.

978 **Appendix A. Kinematics**

979 Some plots of kinematics relevant to the OLYMPUS experiment and elas-
 980 tic lepton-proton scattering at a beam energy of 2.01 GeV are given below.
 981 The straight lines indicate the nominal angular coverage of the wire cham-
 bers, 20°–80°, and the centerline of the 12° detector telescopes.

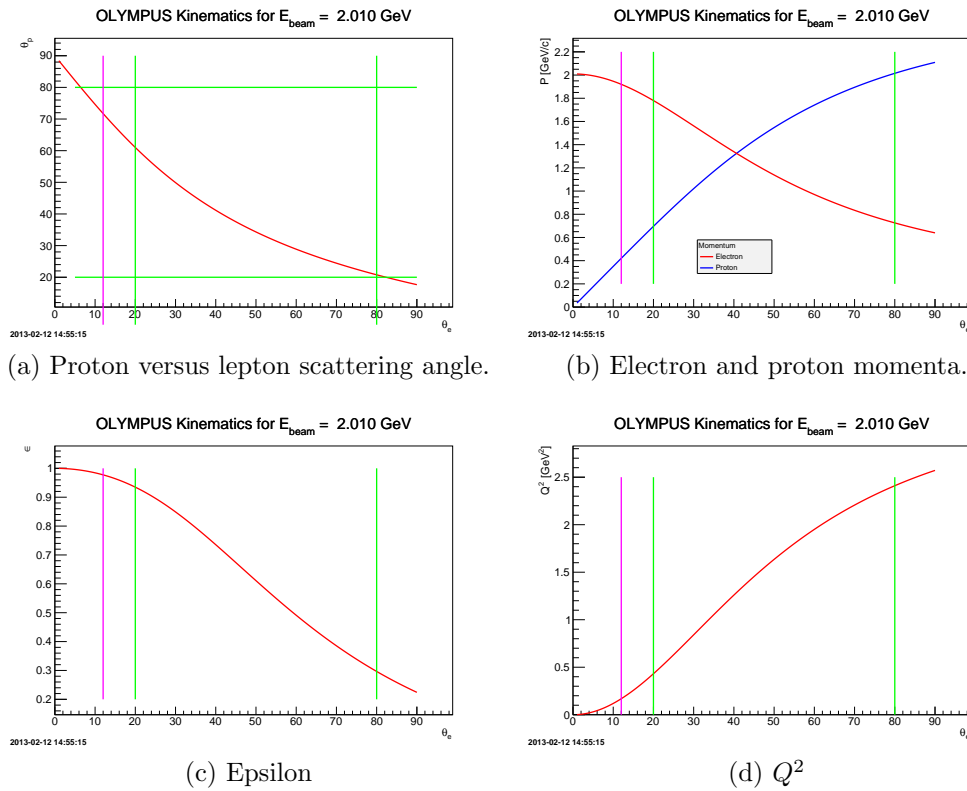
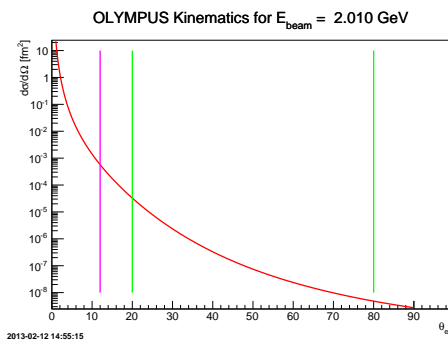
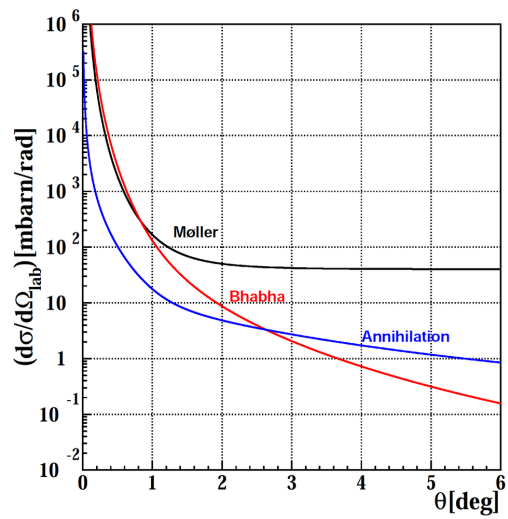


Fig. A.32

982



(e) Elastic ep cross section assuming dipole form factors.



(f) Symmetric Møller, Bhabha, and annihilation cross sections.

Fig. A.32

983 **References**

- 984 [1] A. J. R. Puckett, others, Recoil Polarization Measurements of the Proton
985 Electromagnetic Form Factor Ratio to $Q^2 = 8.5 \text{ GeV}^2$, Phys. Rev. Lett.
986 104 (2010) 242301.
- 987 [2] M. Paolone, S. P. Malace, S. Strauch, I. Albayrak, J. Arrington, oth-
988 ers, Polarization Transfer in the ${}^4\text{He}(\vec{e}, e'\vec{p}){}^3\text{H}$ Reaction at $Q^2 = 0.8$ and
989 1.3 (GeV/c)^2 , Phys. Rev. Lett. 105 (2010) 072001.
- 990 [3] B. Hu, others, Polarization transfer in the ${}^2\text{H}(\vec{e}, e'\vec{p})n$ reaction up to Q^2
991 $= 1.61 \text{ (GeV/c)}^2$, Phys. Rev. C73 (2006) 064004.
- 992 [4] M. K. Jones, others, G_{E_p}/G_{M_p} Ratio by Polarization Transfer in $\vec{e}p \rightarrow$
993 $e\vec{p}$, Phys. Rev. Lett. 84 (2000) 1398–1402.
- 994 [5] G. MacLachlan, others, The ratio of proton electromagnetic form factors
995 via recoil polarimetry at $Q^2 = 1.13 \text{ (GeV/c)}^2$, Nucl. Phys. A764 (2006)
996 261–273.
- 997 [6] V. Punjabi, others, Proton elastic form factor ratios to $Q^2 = 3.5 \text{ GeV}^2$
998 by polarization transfer, Phys. Rev. C71 (2005) 055202.
- 999 [7] S. Strauch, others, Polarization Transfer in the ${}^4\text{He}(\vec{e}, e'\vec{p}){}^3\text{H}$ Reaction
1000 up to $Q^2 = 2.6 \text{ (GeV/c)}^2$, Phys. Rev. Lett. 91 (2003) 052301.
- 1001 [8] O. Gayou, others, Measurement of G_{E_p}/G_{M_p} in $\vec{e}p \rightarrow e\vec{p}$ to $Q^2 =$
1002 5.6 GeV^2 , Phys. Rev. Lett. 88 (2002) 092301.
- 1003 [9] I. A. Qattan, others, Precision Rosenbluth measurement of the proton
1004 elastic form factors, Phys. Rev. Lett. 94 (2005) 142301.
- 1005 [10] M. E. Christy, others, Measurements of electron-proton elastic cross
1006 sections for $0.4 < Q^2 < 5.5 \text{ (GeV/c)}^2$, Phys. Rev. C70 (2004) 015206.
- 1007 [11] L. Andivahis, others, Measurements of the electric and magnetic form
1008 factors of the proton from $Q^2 = 1.75$ to 8.83 (GeV/c)^2 , Phys. Rev. D50
1009 (1994) 5491–5517.
- 1010 [12] R. C. Walker, B. W. Filippone, J. Jourdan, R. Milner, R. McKe-
1011 own, D. Potterveld, L. Andivahis, R. Arnold, D. Benton, P. Bosted,

- 1012 G. deChambrier, A. Lung, S. E. Rock, Z. M. Szalata, A. Para, F. Diet-
1013 rich, K. Van Bibber, J. Button-Shafer, B. Debebe, R. S. Hicks, S. Dasu,
1014 P. de Barbaro, A. Bodek, H. Harada, M. W. Krasny, K. Lang, E. M. Ri-
1015 ordan, Measurements of the proton elastic form factors for $1 \leq Q^2 \leq 3$
1016 $(\text{GeV}/c)^2$ at SLAC, Phys. Rev. D49 (11) (1994) 5671–5689.
- 1017 [13] P. A. Guichon, M. Vanderhaeghen, How to reconcile the Rosenbluth
1018 and the polarization transfer method in the measurement of the proton
1019 form-factors, Phys.Rev.Lett. 91 (2003) 142303. arXiv:hep-ph/0306007,
1020 doi:10.1103/PhysRevLett.91.142303.
- 1021 [14] P. Blunden, W. Melnitchouk, J. Tjon, Two photon exchange and elastic
1022 electron proton scattering, Phys.Rev.Lett. 91 (2003) 142304. arXiv:nucl-
1023 th/0306076, doi:10.1103/PhysRevLett.91.142304.
- 1024 [15] Y. C. Chen, A. Afanasev, S. J. Brodsky, C. E. Carlson, M. Vander-
1025 haeghen, Partonic calculation of the two-photon exchange contribution
1026 to elastic electron-proton scattering at large momentum transfer, Phys.
1027 Rev. Lett. 93 (12) (2004) 122301. doi:10.1103/PhysRevLett.93.122301.
- 1028 [16] A. V. Afanasev, S. J. Brodsky, C. E. Carlson, Y.-C. Chen, M. Vander-
1029 haeghen, Two-photon exchange contribution to elastic electron-nucleon
1030 scattering at large momentum transfer, Phys. Rev. D 72 (1) (2005)
1031 013008. doi:10.1103/PhysRevD.72.013008.
- 1032 [17] P. G. Blunden, W. Melnitchouk, J. A. Tjon, Two-photon exchange in
1033 elastic electron-nucleon scattering, Phys. Rev. C 72 (3) (2005) 034612.
1034 doi:10.1103/PhysRevC.72.034612.
- 1035 [18] S. Kondratyuk, P. G. Blunden, W. Melnitchouk, J. A. Tjon,
1036 Δ resonance contribution to two-photon exchange in electron-
1037 proton scattering, Phys. Rev. Lett. 95 (17) (2005) 172503.
1038 doi:10.1103/PhysRevLett.95.172503.
- 1039 [19] E. Tomasi-Gustafsson, G. Gakh, Search for evidence of two photon con-
1040 tribution in elastic electron proton data, Phys.Rev. C72 (2005) 015209.
1041 arXiv:hep-ph/0412137, doi:10.1103/PhysRevC.72.015209.
- 1042 [20] Y. M. Bystritskiy, E. A. Kuraev, E. Tomasi-Gustafsson, Structure func-
1043 tion method applied to polarized and unpolarized electron-proton scat-
1044 tering: A solution of the $G_E(p)/G_M(p)$ discrepancy, Phys. Rev. C 75

- 1045 (2007) 015207. doi:10.1103/PhysRevC.75.015207.
1046 URL <http://link.aps.org/doi/10.1103/PhysRevC.75.015207>
- 1047 [21] Y.-C. Chen, C.-W. Kao, S.-N. Yang, Is there model-independent evi-
1048 dence of the two-photon-exchange effect in the electron-proton elastic
1049 scattering cross-section?, *Phys.Lett. B* 652 (2007) 269–274. arXiv:nucl-
1050 th/0703017, doi:10.1016/j.physletb.2007.07.044.
- 1051 [22] J. Guttmann, N. Kivel, M. Meziane, M. Vanderhaeghen, Determination
1052 of two-photon exchange amplitudes from elastic electron-proton scatter-
1053 ing data, *The European Physical Journal A - Hadrons and Nuclei* 47
1054 (2011) 1–5, 10.1140/epja/i2011-11077-4.
1055 URL <http://dx.doi.org/10.1140/epja/i2011-11077-4>
- 1056 [23] M. Gorchtein, Dispersive contributions to e^+p/e^-p cross section ratio in
1057 forward regime, *Physics Letters B* 644 (5-6) (2007) 322–330. doi:DOI:
1058 10.1016/j.physletb.2006.11.065.
1059 URL <http://www.sciencedirect.com/science/article/pii/S0370269306015231>
- 1060 [24] D. Borisyuk, A. Kobushkin, Box diagram in the elastic electron-
1061 proton scattering, *Phys.Rev. C* 74 (2006) 065203. arXiv:nucl-th/0606030,
1062 doi:10.1103/PhysRevC.74.065203.
- 1063 [25] H. Albrecht, others, Physics with ARGUS, *Phys. Rept.* 276 (1996) 223–
1064 405.
- 1065 [26] D. Hasell, T. Akdogan, R. Alarcon, W. Bertozzi, E. Booth, others, The
1066 BLAST experiment, *Nucl. Instrum. Meth. A* 603 (2009) 247–262.
- 1067 [27] K. A. Dow, T. Botto, A. Goodhue, D. K. Hasell, D. Loughnan, oth-
1068 ers, Magnetic field measurements of the BLAST spectrometer, *Nucl.*
1069 *Instrum. Meth. A* 599 (2009) 146–151.
- 1070 [28] F. Simon, J. Kelsey, K. M. R. Majka, M. Plesko, T. Sakuma, N. Smirnov,
1071 H. Spinka, B. Surrow, S. Underwood, Beam performance of tracking
1072 detectors with industrially produced gem foils, *Nucl. Instrum. Meth.*
1073 *A* 598 (2009) 432–438.
- 1074 [29] M. J. French, others, Design and results from the APV25, a deep sub-
1075 micron CMOS front-end chip for the CMS tracker, *Nucl. Instrum. Meth.*
1076 *A* 466 (2001) 359–365.

- 1077 [30] N. Bondar, V. Golovtsov, A. Golyash, E. Lobachev, L. Uvarov,
1078 S. Uvarov, V. Yatsura, Third Generation Coordinate ReadOut System
1079 CROS-3, PNPI High Energy Physics Division Main Scientific Activities
1080 2002-2006 (2007) 334.
- 1081 [31] A. Andreev, S. Belostotsky, G. Gavrilov, O. Grebenyuk, E. Ivanov, oth-
1082 ers, Multiwire proportional chambers in the HERMES experiment, Nucl.
1083 Instrum. Meth. A465 (2001) 482–497.
- 1084 [32] R. Veenhof, GARFIELD, recent developments, Nucl. Instrum. Meth.
1085 A419 (1998) 726–730.
- 1086 [33] R. Kothe, Design and operation of fast calorimeter electronics for an
1087 experiment for the measurement of the parity violation in elastic electron
1088 scattering.
- 1089 [34] D. M. Piontek, The new online monitor for the Crystal Barrel Exper-
1090 iment at ELSA, 24th Students' Workshop on Electromagnetic Interac-
1091 tions Bosen (Saar), 2006.